



# Resolving multiple geological events using *in situ* Rb-Sr geochronology: implications for metallogenesis at Tropicana, Western Australia

5 Hugo K. H. Olierook<sup>1,2,3\*</sup>, Kai Rankenburg<sup>1,3</sup>, Stanislav Ulrich<sup>4</sup>, Christopher L. Kirkland<sup>1,2</sup>, Noreen J. Evans<sup>1,3</sup>, Stephen Brown<sup>4</sup>, Brent I. McInnes<sup>3</sup>, Alexander Prent<sup>1,3</sup>, Jack Gillespie<sup>1</sup>, Bradley McDonald<sup>1</sup>, and Miles Darragh<sup>4</sup>

<sup>1</sup>School of Earth and Planetary Sciences, Curtin University, GPO Box U1987, Perth, WA 6845, Australia

<sup>2</sup>Centre for Exploration Targeting – Curtin Node, Curtin University, GPO Box U1987, Perth, WA 6845, Australia

<sup>3</sup>John de Laeter Centre, Curtin University, GPO Box U1987, Perth, WA 6845, Australia

10 <sup>4</sup>AngloGold Ashanti Australia Ltd., 140 St. Georges Terrace, Perth, WA 6000, Australia

Correspondence to: Hugo K. H. Olierook ([hugo.olierook@curtin.edu.au](mailto:hugo.olierook@curtin.edu.au))

**Abstract.** Dating multiple geological events in single samples using thermochronology and geochronology is relatively  
15 common but it is only with the recent advent of triple quadrupole LA-ICP-MS that *in situ* Rb-Sr dating has become a more commonly applied and powerful tool to date K- and Rb-bearing minerals. Here, we date, for the first time, two generations of mineral assemblages in individual thin sections using the *in situ* Rb-Sr method. Two distinct mineral assemblages, both probably associated with Au mineralization, are identified in samples from the Tropicana gold mine in the Albany–Fraser Orogen, Western Australia. For Rb-Sr purposes, the key dateable minerals are two generations of biotite, and additional  
20 phengite associated with the second assemblage. Our results reveal that the first, coarse-grained generation of biotite grains records a minimum age of  $2535 \pm 18$  Ma, coeval with previous  $^{40}\text{Ar}/^{39}\text{Ar}$  biotite, Re-Os pyrite and U-Pb rutile results. The second, fine-grained and recrystallized generation of biotite grains record an age of  $1207 \pm 12$  Ma across all samples. Phengite and muscovite yielded broadly similar results at ca. 1.2 Ga but data is overdispersed for a single coeval population of phengite and shows elevated age uncertainties for muscovite. We propose that the ca. 2530 Ma age recorded by various geochronometers  
25 represents cooling and exhumation, and that the age of ca. 1210 Ma is related to major shearing associated with the regional deformation associated with Stage II of the Albany–Fraser Orogeny. This is the first time that an age of ca. 1210 Ma has been identified in the Tropicana Zone, which may have ramifications for constraining the timing of mineralization in the region. The *in situ* Rb-Sr technique is currently the only tool capable of resolving both geological events in these rocks.



## 30 1.0 Introduction

The ability to date multiple events in individual samples has important consequences for developing a comprehensive understanding of the geological history of complex terranes. The U-Pb method has long been employed to date crystallization, metamorphism and hydrothermal events, often by targeting cores and rims in individual grains. Many U-bearing minerals have recorded multiple ages due to their ability to participate in metamorphic/hydrothermal reactions or become (partially) reset by events above mineral closure temperatures, including zircon (Liu et al., 2012), monazite (Rasmussen et al., 2007), titanite (Olierook et al., 2019), rutile (Zack and Kooijman, 2017) and apatite (Kirkland et al., 2018). However, not all geological events are associated with (partial) reset or new growth of U-bearing minerals. In these scenarios, it is important to examine alternative minerals that may provide a more complete record of the geological history.

40 The Rb-Sr isotopic system is particularly valuable for geochronology, as Rb is sufficiently abundant in common K-bearing minerals like biotite, muscovite and K-feldspar that are abundant in a wide variety of rocks, and are readily mobilized during fluid-rock interactions (Riley and Compston, 1962; Attendorf and Bowen, 1997).  $^{87}\text{Sr}$  decays to  $^{87}\text{Rb}$  with a recently revised decay constant of  $1.3972 \pm 0.0045 \times 10^{-11}$  a (equivalent to half-life of  $\sim 49.6$  Ga; Villa et al., 2015). However, the most significant disadvantage of traditional Rb-Sr geochronology is the inability to perform *in situ* dating via secondary ion mass spectrometry (SIMS) or laser ablation inductively coupled plasma mass spectrometry (LA-ICP-MS; Nebel, 2013). Although several studies have dated mineral separates on a small scale (Glodny et al., 2002; Glodny et al., 2003), some even texturally-constrained by micromilling (Chen et al., 1996; Charlier et al., 2006), the Rb-Sr technique could not compete with the  $<100$   $\mu\text{m}$  diameter resolution of the U-Pb method.

50 The major obstacle with *in situ* Rb-Sr geochronology is the isobaric interference of different isotopes, most notably that of  $^{87}\text{Rb}$  and  $^{87}\text{Sr}$  (Zack and Hogmalm, 2016). Pioneering work from Moens et al. (2001) and Vanhaecke et al. (2003) showed that it was possible to achieve chemical separation of interfering  $^{87}\text{Rb}$  from  $^{87}\text{Sr}$  inside a conventional ICP-MS by directing the ion beam through a dynamic reaction cell with  $\text{CH}_3\text{F}$  gas to produce  $\text{SrF}^+$  ( $m/v \approx 106$ ) but leave Rb unaffected ( $m/v \approx 87$ ). However, this technique was relatively imprecise ( $\pm \sim 10\%$ ; Vanhaecke et al., 2003), particularly when compared to *in situ* U-Pb methods ( $< \pm 2\%$ ) and still required dissolution of the sample.

60 With the recent advent of ‘triple quadrupole’ LA-ICP-MS, it is now possible to perform *in situ* Rb-Sr dating at precision that rivals *in situ* U-Pb geochronology (Zack and Hogmalm, 2016; Hogmalm et al., 2017). A reaction cell located between two quadrupoles is filled with a selected gas (e.g.,  $\text{N}_2\text{O}$ ,  $\text{SF}_6$ ,  $\text{O}_2$ ) that reacts with  $\text{Sr}^+$  ions but leaves  $\text{Rb}^+$  unaffected. Thus, the first quadrupole is used to filter ions of a specific mass (e.g.,  $^{87}\text{Rb}$  and  $^{87}\text{Sr}$ ) to enter the reaction cell and the second quadrupole separates the  $^{87}\text{Rb}$  from the reacted (mass-shifted) Sr (e.g.,  $^{87}\text{Sr}^{16}\text{O}$ ; now  $m/v$  103, see supplementary Fig. A for graphic illustration of this process).



65 Following the work of Zack and Hogmalm (2016) and Hogmalm et al. (2017) for assessing the most suitable reaction cell  
gases, several publications have attempted to solve geological problems using the *in situ* Rb-Sr technique (Şengün et al.,  
2019; Tillberg et al., 2017; Tillberg et al., 2020). All these studies, except the one from Tillberg et al. (2020), identified only a  
single age population within individual samples, which could have been resolved (at higher precision) with solution Rb–Sr or  
 $^{40}\text{Ar}/^{39}\text{Ar}$ . Tillberg et al. (2020) observed multiple age populations in their samples, but these were from mineral separates and  
the textural context was not preserved. To date, no published study has taken full advantage of the spatial resolving power of  
70 the *in situ* Rb-Sr technique whilst retaining textural context.

Here, we analyzed in thin sections, the *in situ* Rb-Sr ages of two mineral assemblages developed in distinctly different  
deformation microstructures in the Tropicana Zone of the Albany–Fraser Orogen, southwestern Australia. For Rb-Sr purposes,  
we date (i) biotite from both assemblages, (ii) apatite from both generations, (iii) phengite from assemblage 2, and (iv)  
75 muscovite from assemblage 2. Ultimately, this work demonstrates the use of coupled *in situ* Rb-Sr geochronology and  
microstructural analysis for identifying and resolving multiple geological events in individual samples.

## 2.0 Geological Background

### 2.1 Geological history of the Albany–Fraser Orogen

The Albany-Fraser Orogen is a Proterozoic orogenic belt that girdles ~1200 km of the south and southeastern margins of the  
80 Archean Yilgarn Craton in Western Australia. This belt had a protracted Proterozoic history that included a series of  
extensional and compressional events at ca. 2720–2530 Ma, 1810–1650 Ma and 1330–1140 Ma (Spaggiari et al., 2015). The  
Albany-Fraser Orogen comprises several lithotectonic domains including the Northern Foreland, Tropicana Zone, Biranup  
Zone, Nornalup Zone and Fraser Zone (**Fig. 1**), and principally represents the reworked margin of the Archean Yilgarn Craton  
(Kirkland et al., 2011). Each zone comprises minor to dominant components of Archean heritage variably reworked by  
85 Paleoproterozoic and Mesoproterozoic tectonomagmatic events.

The earliest event in the belt at ca. 2720–2530 Ma was restricted to the Tropicana Zone (see section 2.2) and was followed by  
magmatism from 1.81 Ga to 1.65 Ga in the Tropicana, Biranup and Nornalup zones (Smithies et al., 2015). This earlier  
Paleoproterozoic magmatism is divided into three pulses: Salmon Gums Event (1.81–1.80 Ga), Ngadju Event (1.77–1.75 Ga)  
90 and Biranup Orogeny (1.70–1.65 Ga; Kirkland et al., 2011; Spaggiari et al., 2015; Smithies et al., 2015). The tectonic setting in  
which this significant Paleoproterozoic magmatism occurred is not well constrained, however, it is generally interpreted to  
represent an extensional event (Spaggiari et al., 2015; Hartnady et al., 2019; Smits et al., 2014), with short-lived pulses of  
compression (i.e. Zanthus Event; Kirkland et al., 2011; Smithies et al., 2015).



The majority of the magmatism in the Albany-Fraser Orogen occurred during arc-accretion and subsequent reworking at 1330  
95 Ma and 1200 Ma, respectively (Spaggiari et al., 2015). The Albany-Fraser Orogen shares a heritage with Wilkes Land in East  
Antarctica, and these two orogenic belts were contiguous during the late Mesoproterozoic as a result of Rodinia assembly  
(Morrissey et al., 2017; Clark et al., 2000). Stage I of the Albany-Fraser Orogeny (1330–1260 Ma) was a widespread high-  
temperature, moderate- to high-pressure event accompanied by felsic and mafic magmatism (Clark et al., 2014). Stage I is  
generally interpreted as the collision between the Western Australian and Mawson Craton (Clark et al., 2000; Bodorkos and  
100 Clark, 2004). Stage II of the Albany-Fraser Orogeny is considered to reflect intracratonic orogenesis (Spaggiari et al.,  
2009; Spaggiari et al., 2015; Spaggiari et al., 2014). This stage is associated with craton-verging thrusting, high-temperature  
and moderate-pressure metamorphism, and mainly felsic magmatism at ca. 1225–1140 Ma (Dawson et al., 2003; Nelson et al.,  
1995). Mafic intrusions associated with Stage II are not known in the eastern Albany-Fraser Orogen but have recently been  
documented at  $1134 \pm 9$  (U-Pb zircon) and  $1131 \pm 16$  Ma (U-Pb baddeleyite) in the Bungar Hills, Wilkes Land (Stark et al.,  
105 2018).

## 2.2 Geological and mineralization history of the Tropicana Zone

The Tropicana Zone is located along the northeastern margin of the Yilgarn Craton (Fig. 1). Seismic sections across the  
Tropicana Zone reveal a northwest directed, imbricate thrust stack formed in a foreland setting by thrusting of the Tropicana  
Zone up along a major thrust surface known as the Plumridge Detachment (Occhipinti et al., 2014; Occhipinti et al., 2018).  
110 This thrust transported the Tropicana Zone onto the Yamarna Terrane of the Yilgarn Craton (Occhipinti et al., 2018).

The Tropicana Zone includes the Tropicana gold mine and several prospects to the northeast and southwest (Fig. 1; Occhipinti  
et al., 2018; Spaggiari et al., 2014). A moderately foliated metagranite (Hercules Gneiss) sampled close to the Tropicana gold  
mine yielded a U-Pb age of  $2722 \pm 15$  Ma on oscillatory-zoned zircon cores interpreted to represent the magmatic  
115 crystallization age of the granite (Kirkland et al., 2015). A younger age of  $2640 \pm 10$  Ma on zircon rims from the same sample  
was interpreted as the age of a high-grade metamorphic overprint in the zone. In the Tropicana gold mine itself, a similar  
minimum age of crystallization ( $2638 \pm 4$  Ma) was acquired from the syenitic lithofacies of the Tropicana Gneiss (Doyle et  
al., 2015). The Hercules Gneiss has broadly dioritic compositions and a very narrow range of low  $\text{SiO}_2$  (58.1–63.6 wt%), and  
is classified as a sanukitoid (Kirkland et al., 2015). Sanukitoid magmas, usually are produced from metasomatized mantle in  
120 an arc setting (Martin et al., 2005), are known for gold fertility and are interpreted as a likely source of gold in the Tropicana  
Zone, although the gold may have been remobilised on several occasions (Kirkland et al., 2015). Sanukitoid intrusions  
commenced at  $2692 \pm 16$  Ma near the start of a prolonged mid-amphibolite to lower granulite facies metamorphism in the  
Tropicana Zone that persisted until ca. 2530 Ma (Kirkland et al., 2015; Doyle et al., 2015). Kirkland et al. (2015) interpreted  
the characteristic high-grade metamorphic textures and grain shapes of zircon as evidence of a prolonged period of granulite  
125 facies metamorphism (Atlantis Event) that formed many of the gneisses in the Tropicana Zone. Structural and isotopic data



imply that the Tropicana Zone was held at a deep-crustal level during much of the Neoproterozoic (Tyler et al., 2015; Occhipinti et al., 2018).

Exhumation and retrogression to greenschist facies metamorphic conditions associated with folding and development of thrust  
130 shear zones occurred at ca. 2530 Ma (Blenkinsop and Doyle, 2014; Doyle et al.; Doyle et al., 2015). Thrusting onto the Yilgarn  
Craton is thought to have led to ingress of fluids and Au mineralization at ca. 2530 Ma (Occhipinti et al., 2018; Doyle et al.,  
2015). The age of ca. 2530 Ma from the Tropicana gold mine is constrained from a biotite  $^{40}\text{Ar}/^{39}\text{Ar}$  age of  $2531 \pm 14$  Ma,  
recalculated using the decay constant of Renne et al. (2011), and an imprecise pyrite Re-Os age of ca.  $2505 \pm 50$  Ma.  
Additionally, a tungsten-rich rutile population exsolved from a coarse-grained biotite yielded dates between  $2539 \pm 22$  Ma and  
135  $2479 \pm 10$  Ma, overdispersed for a single population (Doyle et al., 2015). There is evidence from the work of Doyle et al.  
(2015) for subsequent resetting of geochronometers. Although Doyle et al. (2015) advocates for a  $2521 \pm 5$  Ma age for rutile  
formation, it is more likely this represents partial resetting. Similarly, pyrite Pb/Pb results show scatter between ca. 2500 Ma  
and 1800 Ma, disturbed  $^{40}\text{Ar}/^{39}\text{Ar}$  spectra show a range of individual steps between ca. 2.0 and 1.8 Ga and U-Pb zircon and  
140 monazite ages show partial loss of Pb towards Mesoproterozoic ages but with poorly constrained lower intercepts (ca. 1.3–1.1  
Ga). Whether these dates represent distinct events at ca. 2.4, 1.8 Ga and/or 1.3–1.1 Ga or are a continuum of dates towards  
younger ages remains unknown.

### 3.0 Sample selection

The sampling strategy for the Tropicana gold mine followed that of Blenkinsop and Doyle (2014), focusing on the Au-  
mineralized D3 shear zone. There is a natural strain gradient from undeformed syenitic gneiss host rock to transient low-strain,  
145 up to high-strain zones. A total of ten samples were selected from diamond drill cores (photos in Supplementary Fig. B) from  
three main pits in the Tropicana gold mine (Table 1, Figs. 1–2). All samples are perthitic K-feldspar dominated rocks with  
minor biotite and quartz, deformed at low strains to a brittle-ductile microstructure at greenschist facies conditions. Additional  
phases include albitized plagioclase, biotite, phengite, quartz, calcite/dolomite, pyrite, zircon and monazite (Supplementary  
Fig. B).

150 Three samples were selected from satellite prospects proximal to the Tropicana gold mine and within the Tropicana Zone, one  
each from the New Zebra, Iceberg and Angel Eyes prospects (Table 1, Figs. 1–2). The sample from the New Zebra prospect  
displays parasitic folding defined by muscovite and quartz (Table 1, Supplementary Fig. B). The Iceberg and Angel Eyes  
samples are both strongly foliated, with foliation defined by quartz, phengite  $\pm$  altered plagioclase (Table 1, Supplementary  
155 Fig. B).



A subset of four of the ten samples from the Tropicana gold mine were selected for *in situ* Rb-Sr geochronology (Table 1, Figs. 1–2). From the satellite prospects, the sample from the New Zebra prospect was selected.

## 160 4.0 Methods

### 4.1 Thin section preparation and imaging

Standard polished thin sections prepared at Minerex Services, Esperance, Western Australia, were imaged in plane- and cross-polarized, transmitted light on an Axio II optical microscope at the School of Earth and Planetary Sciences, Curtin University. Thin sections were subsequently carbon coated and analyzed using a Tescan Integrated Mineral Analyser (TIMA) at the John de Laeter Centre (JdLC) at Curtin University to aid in mineral identification. TIMA (a field emission gun scanning electron microscopy) is equipped with four electron dispersive X-ray spectrometers (EDS), capable of recording 420k X-ray counts per second. Thin sections were analyzed in ‘dot-mapping’ mode with a rectangular mesh at a step-size of 3  $\mu\text{m}$  for backscattered electron (BSE) imaging. One thousand EDS counts are collected every 9<sup>th</sup> step (i.e., 27  $\mu\text{m}$ ) or when the BSE contrast changes (i.e., a change in mineral phase). For a given mineral grain, EDS counts are integrated across the entire grain. TIMA analyses used an accelerating voltage of 25 kV, a beam intensity of 19, a probe current of 6.74–7.01 nA, a spot size of 67–90 nm and a nominal working distance of 15 mm. After imaging and EDS collection, BSE signals and EDS peaks are referenced to a mineral library for automatic mineral classification.

Full thin section photomicrographs and TIMA images of each sample are in Supplementary Fig. B.

175

### *In situ* Rb-Sr geochronology

*In situ* Rb-Sr data were collected on sample thin sections in the GeoHistory Facility, JdLC, Curtin University, across three sessions. For all sessions, a RESolution LR 193 nm ArF excimer laser with Laurin Technic S155 sample cell was used. Laser settings comprised a beam diameter of 87  $\mu\text{m}$  (session 1) or 64  $\mu\text{m}$  (sessions 2–3), on-sample energy of 2.5 J  $\text{cm}^{-2}$ , a repetition rate of 5 Hz, 60s of analysis time and 30s of on-peak background acquisition with the laser off. All analyses were preceded by two cleaning pulses. Laser fluence was calibrated each day using a hand held energy meter, and subsequent analyses were performed in constant fluence mode. The Laurin Technic S155 sample cell was flushed with ultrahigh purity He (320 mL  $\text{min}^{-1}$ ) with added  $\text{N}_2$  (1.2 mL  $\text{min}^{-1}$ ), both of which were passed through an inline Hg trap. High purity Ar was used as the ICP-MS carrier gas (flow rate  $\sim 1$  L  $\text{min}^{-1}$ ).

185

Rb-Sr data were collected on an Agilent 8900 triple quadrupole mass spectrometer in MS/MS mode (see Supplementary Table A for all relevant tuning and acquisition parameters) using  $\text{N}_2\text{O}$  reaction gas following the pioneering work of Cheng et al. (2008) and Hogmalm et al. (2017). Each analytical session consisted of first tuning gas flows and ICP-MS ion lenses in single



quad mode for sensitivity and a flat mass response curve, followed by adjustment for robust plasma conditions, including  
190  $^{238}\text{U}/^{232}\text{Th} \sim 1$ ,  $^{206}\text{Pb}/^{238}\text{U} \sim 0.2$  and  $^{238}\text{UO}/^{238}\text{U} < 0.004$  on NIST610 glass (Kent et al., 2004). The mass spectrometer was then  
set to MS/MS mode, and  $\text{N}_2\text{O}$  was added ( $\sim 0.25$  mL min; not calibrated<sup>-1</sup>) to the reaction cell. The reaction cell was flushed  
with  $\text{N}_2\text{O}$  for several hours before sample analysis to ensure signal stability. NIST610 was used to tune  $\text{N}_2\text{O}$  to maximise  
intensity at mass 104 ( $^{88}\text{Sr}^{16}\text{O}$ ), while maintaining zero counts at mass 101 ( $^{85}\text{Rb}^{16}\text{O}$ ). Finally, pulse-analog (P/A) conversion  
factors for  $^{88}\text{Sr}^{16}\text{O}$  (as  $^{104}\text{Pd}$ ) and  $^{87,85}\text{Rb}$  were determined in single quad mode on NIST610 reference glass and pressed powder  
195 tablets of phlogopite Mica-Mg, respectively (Govindaraju, 1979; Kröner et al., 1996; Morteani et al., 2013; Hogmalm et al.,  
2017), by varying laser spot sizes and/or laser repetition rate to yield  $\sim 2$  Mcps per analyte.

We designed the analytical protocol to stay below the P/A conversion thresholds for Rb and Sr by reducing ablation spot size,  
laser repetition rate, and /or laser energy. Maximizing count rates for  $^{87,86}\text{Sr}$  implied that  $^{88}\text{Sr}$  was not available for mass bias  
200 correction. We thus followed the approach of Hogmalm et al. (2017) to calibrate  $^{87}\text{Sr}/^{86}\text{Sr}$  directly against NIST610 ( $^{87}\text{Sr}/^{86}\text{Sr}$   
 $= 0.709699 \pm 0.000018$ ; Woodhead and Hergt, 2001) to calculate  $^{87}\text{Rb}/^{86}\text{Sr}$  from certified values at  $2.390 \pm 0.005$  (Woodhead  
and Hergt, 2001). In order to check for matrix sensitivity of measured Sr isotopic compositions using this approach, we  
interspersed a megacrystic plagioclase and a modern shark tooth (apatite) with the samples as external standards. The measured  
results for plagioclase ( $^{87}\text{Sr}/^{86}\text{Sr} = 0.7037 \pm 0.0013$ ; 2SE;  $n = 15$ ) and shark tooth apatite ( $^{87}\text{Sr}/^{86}\text{Sr} = 0.7106 \pm 0.0013$ ; 2SE;  $n$   
205  $= 15$ ) are in excellent agreement with the published Sr isotopic compositions of  $0.70310 \pm 0.00007$  (plagioclase Mir a;  
Rankenburg et al., 2004), and modern marine seawater  $^{87}\text{Sr}/^{86}\text{Sr}$  of  $0.709174 \pm 0.000003$  (McArthur et al., 2006), respectively,  
and attest to the validity of our analytical protocol. Our measured  $^{87}\text{Sr}/^{86}\text{Sr}$  for mica-Mg calibrated against NIST610 over the  
course of this study was  $1.8692 \pm 0.0022$  (2SE,  $n = 28$ ), and we used this value along with a crystallization age of  $519.4 \pm 6.5$   
Ma ( $2\sigma$ ) and initial  $^{87}\text{Sr}/^{86}\text{Sr}$  of  $0.72607 \pm 0.00070$  (Hogmalm et al., 2017) to calculate a mean  $^{87}\text{Rb}/^{86}\text{Sr}$  for mica-Mg of  $156.9$   
210  $\pm 2.3$ , with all errors propagated in quadrature.

Whereas all Rb-Sr isotopic analyses were initially normalized and drift-corrected with factors determined from NIST610, an  
additional matrix correction to  $^{87}\text{Rb}/^{86}\text{Sr}$  was only applied to biotite analyses, with uncertainties on Mica-Mg and the unknown  
analyses propagated in quadrature. These corrections were also applied to phengite and muscovite, but with the caveat that  
215 Mica-Mg may not be a concentration-matched standard for these minerals. Because calculated ages from sample biotite mainly  
depend on accurate determination of the Rb/Sr fractionation factor, a secondary mica standard of known age is highly desirable.  
To this end, analyses of unknowns were additionally bracketed with in-house biotite reference material CK001B ( $422 \pm 6$  Ma;  
Kirkland et al., 2007; Daly et al., 1991). Sample CK001B was collected by Daly et al. (1991) but not dated precisely. Collected  
< 50 km from CK001B and having experienced equivalent Caledonian metamorphism, the age of sample CK009 was  
220 determined from amphibole, whole-rock and biotite Rb-Sr solution analyses (Kirkland et al., 2007). CK009 yielded an age of  
 $422 \pm 6$  Ma ( $n = 5$ , MSWD = 0.57,  $p = 0.68$ ), recalculated using the decay constant of Villa et al. (2015), and an initial  $^{87}\text{Sr}/^{86}\text{Sr}$   
ratio of  $0.7108 \pm 0.0001$  (Kirkland et al., 2007). Repeated analytical results from sessions 1–3 on adjacent spots show no



systematic variation in Rb-Sr age (see supplementary Fig. C). During analytical sessions 1, 2 and 3, sample CK001B yielded biotite ages of  $413 \pm 4$  ( $n = 38$ , MSWD = 1.2,  $p = 0.18$ ),  $414 \pm 5$  ( $n = 38$ , MSWD = 0.99,  $p = 0.49$ ) and  $429 \pm 8$  ( $n = 46$ , MSWD = 0.28,  $p = 1.00$ ), respectively (Supplementary Fig. C). All three sessions yielded a combined age of  $416 \pm 3$  ( $n = 122$ , MSWD = 0.99,  $p = 0.52$ ) with an initial  $^{87}\text{Sr}/^{86}\text{Sr}$  of  $0.714 \pm 0.009$  (Supplementary Fig. C). All of the ages and initial ratios overlap with the published values (Kirkland et al., 2007) within  $2\sigma$  uncertainty.

A small round robin analytical run consisting of ~20 standards preceded analytical runs to monitor long-term stability, and overall data integrity. Data were reduced in Iolite (Paton et al., 2011) and in-house Excel macros. Analyses that crosscut multiple minerals or mineral generations at depth were excluded. Rb-Sr isochrons and ages were computed using Isoplot 4.15 (Ludwig, 2012), with the decay constant after Villa et al. (2015). All uncertainties presented in the text are presented at 95% confidence. Full isotopic data for the samples and reference materials are given in supplementary Table B.

## 5.0 Results

### 5.1 Microstructure and mineral paragenesis from the Tropicana gold mine

In the ten samples from the Tropicana gold mine, two mineral assemblages are identified and linked to two distinct microstructures (Figs. 2, 3). Mineral assemblage 1 comprises perthitic K-feldspar, plagioclase, quartz, euhedral biotite 1 (1<sup>st</sup> generation), apatite 1 (1<sup>st</sup> generation), zircon, monazite and Au-bearing pyrite 1 (1<sup>st</sup> generation). Both Au-bearing pyrite and apatite 1 occur as inclusions in K-feldspar (Fig. 3a, e). Lamellae of rutile within coarse-grained biotite 1 were previously identified by Doyle et al. (2015) but were not observed in this study. The coarse-grained microstructure and associated mineral assemblage 1 is rarely preserved in the ore zone due to the low-temperature and high-strain shearing (Fig. 2a, b, c). However, main rock-forming minerals are preserved either in low-strain domains or as porphyroclasts within mylonites (Fig. 2a, b, c).

The fine-grained microstructure and associated mineral assemblage 2 is related to localized brittle to brittle-ductile strain, overprinting assemblage 1 (D3 of Blenkinsop and Doyle, 2014). The brittle strain affects perthite to form a so-called crackle breccia (Blenkinsop and Doyle, 2014). The brittle-ductile strain has reworked quartz and biotite to form transitional microstructures between jigsaw puzzle breccia and core-and-mantle microstructure (Fig. 2c), while plagioclase broke down to a sericite mesh (Fig. 2a, b, c). Dynamic recrystallization was accompanied by the ingress of hydrothermal fluids that precipitated carbonates, pyrite and phengite (Fig. 2a, b, c) and breaks down perthite to albite along fractures (Fig. 2b). The low-strain microstructure represents the main target for our *in situ* dating of an early biotite 1 and dynamically recrystallized biotite 2 (Fig. 3a-d). In the high-strain zone, sericite forms interconnected matrix to porphyroclasts of perthite, quartz and biotite (Fig. 2d). A potential second generation of apatite (apatite 2) is also found interstitially together with assemblage 2 minerals (Fig. 3f).





## 255 5.2 *In situ* Rb-Sr geochronological data

### 5.2.1 Biotite

Biotite was analyzed from all samples from the Tropicana gold mine (Table 1). According to the mineral paragenesis, biotite was sub-divided into two texturally distinct sub-populations: (i) large, subhedral to euhedral grains associated with assemblage 1, and (ii) recrystallized, fine-grained crystals associated with assemblage 2 (Fig. 3).

260

The older component – texturally part of assemblage 1 – does not define a single population and has relatively low  $^{87}\text{Rb}/^{86}\text{Sr}$  (8–620, mean = 171) compared to assemblage 2 biotite (Fig. 4). Assuming initial  $^{87}\text{Sr}/^{86}\text{Sr}$  ratios of 0.7045–0.7058 (as defined by apatite, see below), the variable Rb-Sr ratios yield broadly linear trends with dates between ca. 2400 and 1500 Ma for the four samples (Fig. 4). However, significant variation is observed in all samples. The analyses with the oldest dates (on average) are from samples with limited presence of recrystallized biotite 2. Conversely, samples with younger dates have a more significant proportion of biotite 2.

265

Spot profiles across two large biotite 1 grains were performed to ascertain if there was systematic age variation from core to rim (Fig. 5). The transects show that there is no significant variation in model ages observed across the large grains, with the exception of some younger dates towards the very edges (e.g., analysis 19 in BSD114-541C or analyses 1–2 in TPD542-371-C) or where fractures were intersected with minor recrystallized biotite 2 (Fig. 5).

270

Analyses from the second phase of biotite (biotite 2) yielded statistically valid isochrons in every sample and shows a wider range of  $^{87}\text{Rb}/^{86}\text{Sr}$  ratios (up to 950, mean = 210, Fig. 4). Ages computed from Rb/Sr isochrons are  $1165 \pm 140$  Ma,  $1227 \pm 100$  Ma,  $1211 \pm 19$  Ma, to  $1208 \pm 36$  Ma for the four samples from the Tropicana gold mine ( $p > 0.05$  in all cases, Fig. 4). For three of the samples where a putative second generation of apatite may be coeval with biotite 2 (see section 5.1), it is possible to compute an isochron with both apatite and biotite 2. Combined apatite and biotite 2 yields isochrons of  $1222 \pm 37$ ,  $1241 \pm 33$  Ma and  $1205 \pm 15$  Ma ( $p > 0.05$  in all cases, Fig. 4) but with ages that overlap in uncertainty if apatite is not used in the calculation. There is no systematic variation in ages between samples or between Tropicana gold mine pits.

275

### 280 5.2.2 Phengite

Phengite was analyzed from three of the four samples from the Tropicana gold mine. Phengite, associated with assemblage 2 in the Tropicana gold mine, yielded single, linear Rb/Sr trends with low to moderate  $^{87}\text{Rb}/^{86}\text{Sr}$  values (0.2–32, mean = 13; Fig. 6). Sample TPD542-371-C yielded a statistically-reliable but imprecise age of  $1212 \pm 98$  Ma ( $n = 6$ , MSWD = 1.3,  $p = 0.28$ , Fig. 6b). The two other samples, both from the Havana Pit, yielded broadly linear trends with age estimates of ca. 1220 and 1280 Ma but with overdispersion for a single population (MSWD = 3.5–3.7,  $p < 0.05$ ; Fig. 6c, d). Notwithstanding the data scatter, on a given sample, the phengite age estimates are similar to those obtained via biotite Rb/Sr (cf. Fig. 4).

285



### 5.2.3 Muscovite

Muscovite was present as euhedral crystals in the New Zebra satellite deposit. Muscovite showed only minor spread in  $^{87}\text{Rb}/^{86}\text{Sr}$  (2.0–3.4, **Fig. 6a**). Consequently, it yielded a statistically-valid but imprecise isochron of  $1255 \pm 170$  Ma ( $n = 37$ , MSWD = 1.14,  $p = 0.26$ ) with an initial  $^{87}\text{Sr}/^{86}\text{Sr}$  intercept of  $0.7116 \pm 0.0062$  (**Fig. 6a**).

### 5.2.4 Apatite

As apatite has negligible Rb, there is no modification of initial  $^{87}\text{Sr}/^{86}\text{Sr}$  from any radiogenic decay of  $^{87}\text{Rb}$ . Thus, the measured  $^{87}\text{Sr}/^{86}\text{Sr}$  is equivalent to the initial  $^{87}\text{Sr}/^{86}\text{Sr}$  ratio at the time of (re)crystallization. Apatite 1 was analyzed in three samples, yielding  $^{87}\text{Sr}/^{86}\text{Sr}_{(i)}$  ratios between  $0.7045 \pm 0.0012$  to  $0.7058 \pm 0.0039$  ( $p > 0.05$  in all samples; Fig. 7a, c, d). Apatite 2 was analyzed in three samples, yielding  $^{87}\text{Sr}/^{86}\text{Sr}_{(i)}$  ratios between  $0.7053 \pm 0.0012$  to  $0.7092 \pm 0.0033$  ( $p > 0.05$  in all samples, Table 1, Fig. 7a, b, d). In the two samples where both assemblages of apatite were analyzed, BSD114-514-C yielded initial  $^{87}\text{Sr}/^{86}\text{Sr}$  that overlapped within  $2\sigma$  error but HDD254-711-C yielded more radiogenic values for apatite 2 compared to apatite 1 (Fig. 7a, d).

## 6.0 Discussion

### 6.1 Ages recorded by the Rb-Sr geochronometers in the Tropicana Zone

Two distinct temporal patterns are identified in the Rb-Sr results (Figs. 4–7). We examine below the two isotopic patterns to evaluate their significance and assess the formation mechanisms.

#### 6.1.1 Assemblage 1: ca. 2530 Ma

The first generation of biotite grains consistently shows a scatter of data and a variation in mean isochron ages, with a strong textural control on these age estimates. Samples with dominantly euhedral biotite grains and minimal recrystallized biotite 2 (e.g., BSD114-541-C) yielded a mean age estimate of ca. 2500 Ma (Fig. 4a). Conversely, where the majority of biotite 1 has been recrystallized to biotite 2 (e.g., HDD077-422-C), the age estimates from biotite 1 are as young as ca. 1500 Ma (Fig. 4c). The most likely explanation for this data scatter is variable loss of Rb and Sr (especially radiogenic  $^{87}\text{Sr}$ ) during (partial) resetting of the Rb-Sr isotopic system (Matheney et al., 1990; Kalt et al., 1994; Evans et al., 1995; Eberlei et al., 2015). The mechanism for this phenomenon is related to the crystallographic position and relative stability of  $^{87}\text{Rb}$  and  $^{86}\text{Sr}$  vs  $^{87}\text{Sr}$ . In trioctahedral micas (e.g., biotite and phlogopite), both  $^{87}\text{Rb}$  (1.72 Å) and  $^{86}\text{Sr}$  (1.44 Å) are situated within a large 12-fold coordinated X-site (Shannon, 1976), where Rb can readily exchange for K and Na, and Sr can exchange with Ca (Zussman, 1979). However, once  $^{87}\text{Rb}$  has decayed to  $^{87}\text{Sr}$  in a K or Na site, there is a significant decrease in ionic radius from 1.72 to 1.44 Å (16%; Shannon, 1976), which makes  $^{87}\text{Sr}$  prone to mobility. Therefore, in fluid-mediated recrystallization during



315 hydrothermal or metamorphic events,  $^{87}\text{Sr}$  can escape more readily from the crystal lattice than  $^{87}\text{Rb}$  or  $^{86}\text{Sr}$  into the percolating fluid.

320 Considering that the excess scatter in the first assemblage biotite grains is due to partial resetting linked to dynamic recrystallization, it follows that the oldest biotite grains can yield a minimum age for the first event. In the samples where the crystals are freshest, coarsest and least overprinted by shearing and assemblage 2, the oldest biotite grains provide a minimum age of  $2535 \pm 18$  Ma for assemblage 1 (Fig. 4a). This is consistent within error with biotite  $^{40}\text{Ar}/^{39}\text{Ar}$  ( $2531 \pm 14$  Ma) and pyrite Re-Os ages ( $2505 \pm 50$  Ma), and broadly compatible with the oldest W-rich rutile U-Pb dates of ca. 2539–2479 Ma obtained from similar samples in the Tropicana gold mine (Fig. 9; Doyle et al., 2015).

### 6.1.2 Assemblage 2: ca. 1210 Ma

325 Ages of the recrystallized biotite grains from assemblage 2 are within uncertainty of one another for all samples from the Tropicana gold mine. Considering the relative proximity of all samples within the Tropicana gold mine, it is unlikely that the duration of a hydrothermal event associated with dynamic recrystallization of biotite would have exceeded the uncertainty of the Rb-Sr geochronometer. We therefore calculate a single weighted mean age of  $1207 \pm 12$  Ma ( $n = 62$ ,  $\text{MSWD} = 0.91$ ,  $p = 0.68$ ) for all available analysis of this fabric (Fig. 8), and consider this age to record a synchronous event across the Tropicana gold mine. Assuming biotite 2 grains were coeval with apatite 2, a better initial  $^{87}\text{Sr}/^{86}\text{Sr}$  intercept can be defined, relative to one generated from a free-regressed biotite 2 isochron. Hence, we have also computed a weighted mean age with apatite 2 and biotite 2 at  $1212 \pm 9$  Ma ( $n = 102$ ,  $\text{MSWD} = 1.3$ ,  $p = 0.05$ ), overlapping within uncertainty with the biotite-only regressed age (Fig. 8).

335 The phengite ages consistently yield similar ages within  $2\sigma$  of the biotite 2 ages, albeit with excess scatter, implying that biotite 2 and phengite are coeval (Figs. 6, 8). This is consistent with the mineral paragenetic sequence (Fig. 2). The overdispersion in the phengite data could be a consequence of heterogeneous minerals or differences in the matrix between the phengite and the phlogopite primary standard Mica-Mg (see section 4.2). Alternatively, the overdispersion may be a real geological phenomenon, implying that phengite formed over a protracted period.

340

The only sample that contained euhedral muscovite, from the New Zebra deposit, yielded an age of  $1255 \pm 170$  Ma that, although imprecise, also overlaps with the second phase of biotite (biotite 2) and the phengite ages (Figs. 4, 6). Thus, all samples point towards a single event at ca. 1210 Ma.

345 The ca. 1210 Ma event could either represent a distinct, fluid-flow episode that recrystallized biotite, formed phengite and yielded muscovite, or it may record an exhumation event that cooled the Rb-Sr geochronometers to below their closure temperatures. The implication with the latter is that the fluid flow event occurred prior to exhumation.



## 6.2 Implications for metamorphic, hydrothermal and mineralization events in the Albany–Fraser Orogen

350 Two ages at ca. 2530 Ma and 1210 Ma have been previously linked to events in the Albany–Fraser Orogen, although the latter had not been previously identified in the Tropicana Zone. The discovery of the Mesoproterozoic age at Tropicana needs to be explored in terms of implications for structural and hydrothermal evolution, and metallogenesis.

The ca. 2530 Ma age is only known from the Tropicana Zone of the Albany–Fraser Orogen (Doyle et al., 2015; Kirkland et al., 355 2015). Previous workers have interpreted the ca. 2530 Ma age as a distinct hydrothermal event at greenschist facies conditions during D3 shearing, which was also associated with Au mineralization (Blenkinsop and Doyle, 2014; Doyle et al., 2015; Occhipinti et al., 2018). This ca. 2530 Ma event is postulated to have followed a protracted period of granulite-facies metamorphism from ca. 2640 to 2530 Ma as part of the Atlantis event (Kirkland et al., 2015; Doyle et al., 2015).

360 Here, we propose an alternative plausible scenario, namely that the ca. 2530 Ma age represents the timing of cooling below the closure temperatures of the various geochronometers, including U-Pb rutile  $\approx$  ca. 2539–2479 Ma, Re-Os pyrite =  $2505 \pm 50$  Ma, Rb-Sr biotite 1  $\geq 2535 \pm 18$  Ma and  $^{40}\text{Ar}/^{39}\text{Ar}$  biotite =  $2531 \pm 14$  Ma (Doyle et al., 2015 and this study). The closure temperatures for these minerals are low to moderate, in decreasing order: (i) Pb diffusion in rutile = 550–650 °C (Ewing et al., 2015; Kooijman et al., 2010), (ii)  $^{187}\text{Os}$  in pyrite closure =  $\sim 500$  °C (Brenan et al., 2000), (iii)  $^{87}\text{Sr}$  diffusion in biotite = 300–375 400 °C (Del Moro et al., 1982), and (iv)  $^{40}\text{Ar}$  diffusion in biotite = 280–350 °C (Harrison et al., 1985). Given that all the geochronometers are all broadly within error of ca. 2530 Ma (this study and Doyle et al., 2015), exhumation at ca. 2530 Ma would have been relatively faster than the preceding  $\sim 120$  m.y. of the Atlantis Event. Such prolonged slow cooling followed by a relatively faster period of cooling is also observed in the core of the Yilgarn Craton (Goscombe et al., 2019). The rate of cooling and exhumation in Tropicana Zone is difficult to ascertain as the uncertainty on the various geochronometers is 370 insufficiently precise to develop a cooling curve. If the ca. 2530 Ma age recorded in the Tropicana Zone represents a cooling age rather than a distinct tectonic event, an important implication is that D3 shearing occurred post-2530 Ma.

We propose that D3 shearing instead occurred at ca. 1210 Ma. There are several lines of evidence to support this interpretation:

- 375 (1) Mineral assemblage 2 associated with the fine-grained microstructure is stable from low- to high-strain zones across the Tropicana gold mine and does not show any reactivation/secondary dynamic recrystallization or mineral re-equilibration to support subsequent reactivation of the shear zone (Blenkinsop and Doyle, 2014). If only a single shearing event is implicated, this would have to occur during the formation of mineral assemblage 2 (i.e., 1210 Ma).
- (2) Rb-Sr profiles across coarse-grained biotite 1 show limited resetting at grain edges, linked to dynamic recrystallization (Fig. 5), and also consistent with a single shearing event (i.e., 1210 Ma).



380 (3) If D3 shearing occurred at ca. 2530 Ma and it was reset at ca. 1210 Ma, one would expect a range of Proterozoic ages  
from biotite 2, which is clearly not the case (Fig. 8). One could argue that previous geochronological studies in the  
Tropicana gold mine pointed towards a potential mineralizing event at ca. 2000–1800 Ma on the basis of disturbed  
 $^{40}\text{Ar}/^{39}\text{Ar}$  spectra and Pb-Pb dates (Doyle et al., 2015). Additionally, quartz vein-related Au mineralization is  
385 implicated at ca. 2100 Ma for the Hercules and Atlantic gold prospects in the Tropicana Zone based on Re-Os pyrite  
model ages (Kirkland et al., 2015). However, it is equally likely that the Pb-Pb and Re-Os pyrite dates (Doyle et al.,  
2015) represent mixed assemblage 1 and 2 populations, and do not represent distinct events. Disturbed  $^{40}\text{Ar}/^{39}\text{Ar}$   
spectra are also notoriously unreliable (Baksi, 2007).

(4) Finally, there is no unequivocal geological evidence for a distinct shearing event at ca. 2530 Ma (Doyle et al., 2015).

390 Our support for D3 shearing at ca. 1210 Ma does not necessarily mean that assemblage 2 was linked to the primary Au  
mineralization in the Tropicana deposit (Fig. 9). Mesoproterozoic orogens are typically poor in orogenic Au deposits across  
the world (e.g., Goldfarb et al., 2001), and the Albany–Fraser Orogen is no exception. Since the discovery of Tropicana in  
2005 (Doyle et al., 2007; Kendall et al., 2007), it remains the only deposit with economic Au mineralization in the Albany-  
Fraser Orogen. Although Tropicana is unlike typical Archean lode gold deposits in the Yilgarn Craton (e.g., gold not directly  
395 associated with quartz and carbonate veining; Kent et al., 1996; Cassidy et al., 1998), the Tropicana Zone experienced long-  
lived granulite facies metamorphism from ca. 2640 to 2530 Ma (Atlantis Event; Doyle et al., 2015; Kirkland et al., 2015). Such  
long-lived metamorphism might have efficiently reworked all textural indicators of primary mineralization. Indeed, a detailed  
microscale study of the gold compartment in the Tropicana gold mine has demonstrated gold and telluride inclusions within  
granulite facies coarse-grained material from assemblage 1 (Hardwick, 2020). Following these observations, it seems that D3  
400 shearing and alteration minerals of assemblage 2 masks the controls on primary gold mineralization.

There are certainly Proterozoic occurrences of sub-economic Au mineralization in the rest of the Tropicana Zone and possibly  
the wider Albany–Fraser Orogen (Figs. 1b, 6a, 9). Gold prospects such as New Zebra, Iceberg or Angel Eyes lack obvious  
Archean events (Fig. 6a) but still show elevated Au. Therefore, it is probable that subordinate, secondary Au mineralization in  
405 the Tropicana Zone is associated with the D3 shearing event and mineral assemblage 2 formation at ca. 1210 Ma (Fig. 9), but  
it is uncertain whether the Au is remobilized from an Archean source or was only introduced into the Mesoproterozoic crust  
at ca. 1210 Ma.

The ca. 1210 Ma event in the Albany–Fraser Orogen is known from both the early stages of the Albany–Fraser Orogeny Stage  
410 II (Clark et al., 2000; Kirkland et al., 2011; Spaggiari et al., 2014) and the widespread intrusions of the Marnda Moorn dyke  
swarm (Wang et al., 2014; Wingate and Pidgeon, 2005; Dawson et al., 2003). We favour the association of the D3 shearing  
with Stage II of the Albany–Fraser Orogeny given the macro- and microstructural characteristics of the Tropicana gold mine.



## 7.0 Conclusions

*In situ* Rb-Sr geochronology from two assemblages of biotite in the Tropicana gold mine yielded ages of  $2535 \pm 18$  Ma and  
415  $1212 \pm 9$  Ma. The former overlaps with  $^{40}\text{Ar}/^{39}\text{Ar}$  biotite, Re-Os pyrite and U-Pb rutile ages obtained in a previous study,  
whilst the latter is the first record of a Mesoproterozoic age in the Tropicana Zone. We propose that the ca 2530 Ma represents  
cooling of the Yilgarn Craton after granulite facies metamorphism and that the ca. 1210 Ma represent a distinct shearing event  
(D3 of Blenkinsop and Doyle, 2014), potentially associated with Au mineralization. Considering the likely association of the  
ca. 1210 Ma event with major shearing, we consider the most likely cause of this Mesoproterozoic event to be Stage II of the  
420 Albany–Fraser Orogeny. At present, the *in situ* Rb-Sr method is the only technique that could have revealed these two age  
populations without foregoing textural context.

## 8.0 Acknowledgements

AngloGold Ashanti Australia is thanked for funding this project. The Tescan Mira3 TIMA with four PulsTor SDD X-ray  
detectors was acquired through Australian Research Council LIEF grant LE140100150. This study was enabled by AuScope  
425 and the Australian Government via the National Collaborative Research Infrastructure Strategy (NCRIS). The 8900 triple  
quadrupole was obtained via funding from the Curtin University Research Office. J. Savage and B. Hardwick are  
acknowledged for constructive discussions about the Tropicana deposit.

## 9.0 References

- Attendorn, H. G., and Bowen, R. N. C.: Rubidium-strontium dating, in: *Radioactive and Stable Isotope Geology*, Springer, 159-191, 1997.
- 430 Baksi, A. K.: A quantitative tool for detecting alteration in undisturbed rocks and minerals—I: Water, chemical weathering, and  
atmospheric argon, *Geological Society of America Special Papers*, 430, 285–303, 10.1130/2007.2430(15), 2007.
- Blenkinsop, T. G., and Doyle, M. G.: Structural controls on gold mineralization on the margin of the Yilgarn craton, Albany–Fraser  
orogen: The Tropicana deposit, Western Australia, *Journal of Structural Geology*, 67, 189-204,  
<https://doi.org/10.1016/j.jsg.2014.01.013>, 2014.
- 435 Bodorkos, S., and Clark, D. J.: Evolution of a crustal-scale transpressive shear zone in the Albany–Fraser Orogen, SW Australia: 2.  
Tectonic history of the Coramup Gneiss and a kinematic framework for Mesoproterozoic collision of the West Australian and  
Mawson cratons, *Journal of Metamorphic Geology*, 22, 713-731, 2004.
- Brenan, J. M., Cherniak, D. J., and Rose, L. A.: Diffusion of osmium in pyrrhotite and pyrite: implications for closure of the Re–Os  
isotopic system, *Earth and Planetary Science Letters*, 180, 399-413, [https://doi.org/10.1016/S0012-821X\(00\)00165-5](https://doi.org/10.1016/S0012-821X(00)00165-5), 2000.
- 440 Cassidy, K. F., Groves, D. I., and McNaughton, N. J.: Late-Archean granitoid-hosted lode-gold deposits, Yilgarn Craton, Western  
Australia: deposit characteristics, crustal architecture and implications for ore genesis, *Ore Geology Reviews*, 13, 65-102, 1998.



- Charlier, B. L. A., Ginibre, C., Morgan, D., Nowell, G. M., Pearson, D. G., Davidson, J. P., and Ottley, C. J.: Methods for the microsampling and high-precision analysis of strontium and rubidium isotopes at single crystal scale for petrological and geochronological applications, *Chemical Geology*, 232, 114-133, 2006.
- 445 Chen, C.-H., DePaolo, D. J., and Lan, C.-Y.: Rb/Sr microchrons in the Manaslu granite: implications for Himalayan thermochronology, *Earth and Planetary Science Letters*, 143, 125-135, 1996.
- Cheng, P., Koyanagi, G. K., and Bohme, D. K.: On the chemical resolution of the  $^{87}\text{Rb} + (s_0)/^{87}\text{Sr} + (s_1)$  isobaric interference: A kinetic search for an optimum reagent, *Analytica chimica acta*, 627, 148-153, 2008.
- Clark, C., Kirkland, C. L., Spaggiari, C. V., Oorschot, C., Wingate, M. T. D., and Taylor, R. J.: Proterozoic granulite formation driven by mafic magmatism: An example from the Fraser Range Metamorphics, Western Australia, *Precambrian Research*, 240, 1-21, <https://doi.org/10.1016/j.precamres.2013.07.024>, 2014.
- 450 Clark, D. J., Hensen, B. J., and Kinny, P. D.: Geochronological constraints for a two-stage history of the Albany–Fraser Orogen, Western Australia, *Precambrian Research*, 102, 155-183, [http://dx.doi.org/10.1016/S0301-9268\(00\)00063-2](http://dx.doi.org/10.1016/S0301-9268(00)00063-2), 2000.
- Daly, J. S., Aitchison, S. J., Cliff, R. A., Gayer, R. A., and Rice, A. H. N.: Geochronological evidence from discordant plutons for a late Proterozoic orogen in the Caledonides of Finnmark, northern Norway, *Journal of the Geological Society*, 148, 29-40, 1991.
- 455 Dawson, G. C., Krapež, B., Fletcher, I. R., McNaughton, N. J., and Rasmussen, B.: 1.2 Ga thermal metamorphism in the Albany–Fraser Orogen of Western Australia: consequence of collision or regional heating by dyke swarms?, *Journal of the Geological Society*, 160, 29-37, 10.1144/0166-764901-119, 2003.
- Del Moro, A., Puxeddu, M., di Brozolo, F. R., and Villa, I. M.: Rb-Sr and K-Ar ages on minerals at temperatures of 300°–400° C from deep wells in the Larderello geothermal field (Italy), *Contributions to Mineralogy and Petrology*, 81, 340-349, 10.1007/BF00371688, 1982.
- 460 Doyle, M., Savage, J., Blenkinsop, T. G., Crawford, A., and McNaughton, N.: Tropicana: Unravelling the complexity of a+ 6 million ounce gold deposit hosted in granulite facies metamorphic rocks, *World Gold 2013*, Melbourne, 2013 87-94,
- Doyle, M. G., Kendall, B. M., and Gibbs, D.: Discovery and characteristics of the Tropicana gold district, *Geoscience Australia Record* 465 2007/14, 186-190, 2007.
- Doyle, M. G., Fletcher, I. R., Foster, J., Large, R. R., Mathur, R., McNaughton, N. J., Meffre, S., Muhling, J. R., Phillips, D., and Rasmussen, B.: Geochronological constraints on the Tropicana gold deposit and Albany-Fraser orogen, Western Australia, *Economic Geology*, 110, 355-386, 2015.
- Eberlei, T., Habler, G., Wegner, W., Schuster, R., Körner, W., Thöni, M., and Abart, R.: Rb/Sr isotopic and compositional retentivity of muscovite during deformation, *Lithos*, 227, 161-178, <https://doi.org/10.1016/j.lithos.2015.04.007>, 2015.
- 470 Evans, J. A., Millar, I. L., and Noble, S. R.: Hydration during uplift is recorded by reset Rb–Sr whole-rock ages, *Journal of the Geological Society*, 152, 209-212, 1995.



- Ewing, T. A., Rubatto, D., Beltrando, M., and Hermann, J.: Constraints on the thermal evolution of the Adriatic margin during Jurassic continental break-up: U–Pb dating of rutile from the Ivrea–Verbano Zone, Italy, *Contributions to Mineralogy and Petrology*, 169, 44, 475, [10.1007/s00410-015-1135-6](https://doi.org/10.1007/s00410-015-1135-6), 2015.
- Glodny, J., Bingen, B., Austrheim, H., Molina, J. F., and Rusin, A.: Precise eclogitization ages deduced from Rb/Sr mineral systematics: the Maksyutov complex, Southern Urals, Russia, *Geochimica et Cosmochimica Acta*, 66, 1221–1235, 2002.
- Glodny, J., Austrheim, H., Molina, J. F., Rusin, A. I., and Seward, D.: Rb/Sr record of fluid-rock interaction in eclogites: The Marun-Keu complex, Polar Urals, Russia, *Geochimica et Cosmochimica Acta*, 67, 4353–4371, 2003.
- 480 Goldfarb, R. J., Groves, D. I., and Gardoll, S.: Orogenic gold and geologic time: a global synthesis, *Ore Geology Reviews*, 18, 1–75, [https://doi.org/10.1016/S0169-1368\(01\)00016-6](https://doi.org/10.1016/S0169-1368(01)00016-6), 2001.
- Goscombe, B., Foster, D. A., Blewett, R., Czarnota, K., Wade, B., Groenewald, B., and Gray, D.: Neoproterozoic metamorphic evolution of the Yilgarn Craton: A record of subduction, accretion, extension and lithospheric delamination, *Precambrian Research*, 335, 105441, <https://doi.org/10.1016/j.precamres.2019.105441>, 2019.
- 485 Govindaraju, K.: Report (1968–1978) on two mica reference samples: biotite Mica-Fe and phlogopite Mica-Mg, *Geostandards Newsletter*, 3, 3–24, 1979.
- Hardwick, B.: Mineralised textures at the Tropicana Gold Mine, Western Australia: Implications for genetic model and deportment of gold, MSc, University of Tasmania, Hobart, Tasmania, 2020.
- Harrison, T. M., Duncan, I., and McDougall, I.: Diffusion of  $^{40}\text{Ar}$  in biotite: Temperature, pressure and compositional effects, *Geochimica et Cosmochimica Acta*, 49, 2461–2468, [https://doi.org/10.1016/0016-7037\(85\)90246-7](https://doi.org/10.1016/0016-7037(85)90246-7), 1985.
- 490 Hartnady, M. I. H., Kirkand, C. L., Smithies, R. H., Poujol, M., and Clark, C.: Periodic Paleoproterozoic calc-alkaline magmatism at the south eastern margin of the Yilgarn Craton; implications for Nuna configuration, *Precambrian Research*, 332, 105400, <https://doi.org/10.1016/j.precamres.2019.105400>, 2019.
- Hogmalm, K. J., Zack, T., Karlsson, A. K. O., Sjöqvist, A. S. L., and Garbe-Schönberg, D.: In situ Rb–Sr and K–Ca dating by LA-ICP-MS/MS: an evaluation of  $\text{N}_2\text{O}$  and  $\text{SF}_6$  as reaction gases, *Journal of Analytical Atomic Spectrometry*, 32, 305–313, 2017.
- 495 Kalt, A., Grauert, B., and Baumann, A.: Rb-Sr and U-Pb isotope studies on migmatites from the Schwarzwald (Germany): constraints on isotopic resetting during Variscan high-temperature metamorphism, *Journal of Metamorphic Geology*, 12, 667–680, 1994.
- Kendall, B. M., Doyle, M. G., and Gibbs, D.: Tropicana: The discovery of a new gold province in Western Australia, 2007 NewGenGold Conference, November 19, 2007, Perth, Australia, 2007, 85–95,
- 500 Kent, A. J. R., Cassidy, K. F., and Mark Fanning, C.: Archean gold mineralization synchronous with the final stages of cratonization, Yilgarn Craton, Western Australia, *Geology*, 24, 879–882, 1996.
- Kent, A. J. R., Jacobsen, B., Peate, D. W., Waight, T. E., and Baker, J. A.: Isotope Dilution MC-ICP-MS Rare Earth Element Analysis of Geochemical Reference Materials NIST SRM 610, NIST SRM 612, NIST SRM 614, BHVO-2G, BHVO-2, BCR-2G, JB-2, WS-E, W-2, AGV-1 and AGV-2, *Geostandards and Geoanalytical Research*, 28, 417–429, [10.1111/j.1751-908X.2004.tb00760.x](https://doi.org/10.1111/j.1751-908X.2004.tb00760.x), 2004.





- 505 Kirkland, C. L., Daly, J. S., Eide, E. A., and Whitehouse, M. J.: Tectonic evolution of the Arctic Norwegian Caledonides from a texturally- and structurally-constrained multi-isotopic (Ar-Ar, Rb-Sr, Sm-Nd, U-Pb) study, *American Journal of Science*, 307, 459-526, 10.2475/02.2007.06, 2007.
- Kirkland, C. L., Spaggiari, C. V., Pawley, M. J., Wingate, M. T. D., Smithies, R. H., Howard, H. M., Tyler, I. M., Belousova, E. A., and Poujol, M.: On the edge: U–Pb, Lu–Hf, and Sm–Nd data suggests reworking of the Yilgarn craton margin during formation of the Albany-Fraser Orogen, *Precambrian Research*, 187, 223-247, <https://doi.org/10.1016/j.precamres.2011.03.002>, 2011.
- 510 Kirkland, C. L., Spaggiari, C. V., Smithies, R. H., Wingate, M. T. D., Belousova, E. A., Gréau, Y., Sweetapple, M. T., Watkins, R., Tessalina, S., and Creaser, R.: The affinity of Archean crust on the Yilgarn—Albany–Fraser Orogen boundary: implications for gold mineralisation in the Tropicana Zone, *Precambrian Research*, 266, 260-281, 2015.
- Kirkland, C. L., Yakymchuk, C., Szilas, K., Evans, N., Hollis, J., McDonald, B., and Gardiner, N. J.: Apatite: a U-Pb thermochronometer or geochronometer?, *Lithos*, 318-319, 143-157, <https://doi.org/10.1016/j.lithos.2018.08.007>, 2018.
- 515 Kooijman, E., Mezger, K., and Berndt, J.: Constraints on the U–Pb systematics of metamorphic rutile from in situ LA-ICP-MS analysis, *Earth and Planetary Science Letters*, 293, 321-330, <http://dx.doi.org/10.1016/j.epsl.2010.02.047>, 2010.
- Kröner, A., Braun, I., and Jaeckel, P.: Zircon geochronology of anatectic melts and residues from a highgrade pelitic assemblage at Ihosy, southern Madagascar: evidence for Pan-African granulite metamorphism, *Geological Magazine*, 133, 311-323, 1996.
- 520 Liu, L., Wang, C., Cao, Y.-T., Chen, D.-L., Kang, L., Yang, W.-Q., and Zhu, X.-H.: Geochronology of multi-stage metamorphic events: Constraints on episodic zircon growth from the UHP eclogite in the South Altyn, NW China, *Lithos*, 136, 10-26, 2012.
- Ludwig, K.: User’s manual for Isoplot version 3.75–4.15: a geochronological toolkit for Microsoft, Excel Berkley Geochronological Center Special Publication, 2012.
- Martin, H., Smithies, R. H., Rapp, R., Moyen, J. F., and Champion, D.: An overview of adakite, tonalite–trondhjemite–granodiorite (TTG), and sanukitoid: relationships and some implications for crustal evolution, *Lithos*, 79, 1-24, <https://doi.org/10.1016/j.lithos.2004.04.048>, 2005.
- 525 Matheney, R. K., Brookins, D. G., Wallin, E. T., Shafiqullah, M., and Damon, P. E.: Incompletely reset Rb–Sr systems from a Cambrian red-rock granophyre terrane, Florida Mountains, New Mexico, U.S.A, *Chemical Geology: Isotope Geoscience section*, 86, 29-47, [https://doi.org/10.1016/0168-9622\(90\)90004-V](https://doi.org/10.1016/0168-9622(90)90004-V), 1990.
- 530 McArthur, J. M., Rio, D., Massari, F., Castradori, D., Bailey, T. R., Thirlwall, M., and Houghton, S.: A revised Pliocene record for marine-<sup>87</sup>Sr/<sup>86</sup>Sr used to date an interglacial event recorded in the Cockburn Island Formation, Antarctic Peninsula, *Palaeogeography, Palaeoclimatology, Palaeoecology*, 242, 126-136, <https://doi.org/10.1016/j.palaeo.2006.06.004>, 2006.
- Moens, L. J., Vanhaecke, F. F., Bandura, D. R., Baranov, V. I., and Tanner, S. D.: Elimination of isobaric interferences in ICP-MS, using ion–molecule reaction chemistry: Rb/Sr age determination of magmatic rocks, a case study, *Journal of Analytical Atomic Spectrometry*, 16, 991-994, 2001.
- 535



- Morrissey, L. J., Payne, J. L., Hand, M., Clark, C., Taylor, R., Kirkland, C. L., and Kylander-Clark, A.: Linking the Windmill Islands, east Antarctica and the Albany–Fraser Orogen: Insights from U–Pb zircon geochronology and Hf isotopes, *Precambrian Research*, 293, 131-149, <https://doi.org/10.1016/j.precamres.2017.03.005>, 2017.
- 540 Morteani, G., Kostitsyn, Y. A., Gilg, H. A., Preinfalk, C., and Razakamanana, T.: Geochemistry of phlogopite, diopside, calcite, anhydrite and apatite pegmatites and syenites of southern Madagascar: evidence for crustal silicocarbonatitic (CSC) melt formation in a Panafrican collisional tectonic setting, *International Journal of Earth Sciences*, 102, 627-645, 10.1007/s00531-012-0832-x, 2013.
- Nebel, O.: Rb–Sr Dating, in: *Encyclopedia of Scientific Dating Methods*, edited by: Rink, W. J., and Thompson, J., Springer Netherlands, Dordrecht, 1-19, 2013.
- 545 Nelson, D. R., Myers, J. S., and Nutman, A. P.: Chronology and evolution of the Middle Proterozoic Albany-Fraser Orogen, Western Australia, *Australian Journal of Earth Sciences*, 42, 481-495, 10.1080/08120099508728218, 1995.
- Occhipinti, S., Doyle, M., Spaggiari, C., Korsch, R., Cant, G., Martin, K., Kirkland, C., Savage, J., Less, T., and Bergin, L.: Preliminary interpretation of the deep seismic reflection line 12GA-T1: northeastern Albany-Fraser Orogen, Albany-Fraser Orogen seismic and magnetotelluric (MT) workshop 2014: extended abstracts (Preliminary edition), 2014, 44-59,
- 550 Occhipinti, S. A., Tyler, I. M., Spaggiari, C. V., Korsch, R. J., Kirkland, C. L., Smithies, R. H., Martin, K., and Wingate, M. T. D.: Tropicana translated: a foreland thrust system imbricate fan setting for c. 2520 Ma orogenic gold mineralization at the northern margin of the Albany–Fraser Orogen, Western Australia, Geological Society, London, Special Publications, 453, 225-245, 2018.
- Olierook, H. K. H., Taylor, R. J. M., Erickson, T. M., Clark, C., Reddy, S. M., Kirkland, C. L., Jahn, I., and Barham, M.: Unravelling complex geologic histories using U–Pb and trace element systematics of titanite, *Chemical Geology*, 504, 105-122, <https://doi.org/10.1016/j.chemgeo.2018.11.004>, 2019.
- 555 Paton, C., Hellstrom, J., Paul, B., Woodhead, J., and Hergt, J.: Iolite: Freeware for the visualisation and processing of mass spectrometric data, *Journal of Analytical Atomic Spectrometry*, 26, 2508-2518, 2011.
- Rankenburg, K., Lassiter, J. C., and Brey, G.: Origin of megacrysts in volcanic rocks of the Cameroon volcanic chain—constraints on magma genesis and crustal contamination, *Contributions to Mineralogy and Petrology*, 147, 129-144, 2004.
- 560 Rasmussen, B., Fletcher, I. R., and Muhling, J. R.: In situ U–Pb dating and element mapping of three generations of monazite: unravelling cryptic tectonothermal events in low-grade terranes, *Geochimica et Cosmochimica Acta*, 71, 670-690, 2007.
- Renne, P. R., Balco, G., Ludwig, K. R., Mundil, R., and Min, K.: Response to the comment by W.H. Schwarz et al. on "Joint determination of  $^{40}\text{K}$  decay constants and  $^{40}\text{Ar}^*/^{40}\text{K}$  for the Fish Canyon sanidine standard, and improved accuracy for  $^{40}\text{Ar}/^{39}\text{Ar}$  geochronology" by PR Renne et al. (2010), *Geochimica et Cosmochimica Acta*, 75, 5097-5100, 2011.
- 565 Riley, G. H., and Compston, W.: Theoretical and technical aspects of Rb–Sr geochronology, *Geochimica et Cosmochimica Acta*, 26, 1255-1281, [https://doi.org/10.1016/0016-7037\(62\)90055-8](https://doi.org/10.1016/0016-7037(62)90055-8), 1962.
- Şengün, F., Bertrandsson Erlandsson, V., Hogmalm, J., and Zack, T.: In situ Rb–Sr dating of K-bearing minerals from the orogenic Akçaabat gold deposit in the Menderes Massif, Western Anatolia, Turkey, *Journal of Asian Earth Sciences*, 185, 104048, <https://doi.org/10.1016/j.jseaes.2019.104048>, 2019.



- Shannon, R. D.: Revised effective ionic radii and systematic studies of interatomic distances in halides and chalcogenides, *Acta crystallographica section A: crystal physics, diffraction, theoretical and general crystallography*, 32, 751-767, 1976.
- Smithies, R., Spaggiari, C., and Kirkland, C.: Building the crust of the Albany-Fraser Orogen; constraints from granite geochemistry, Geological Survey of Western Australia, Perth, WA, 2015.
- Smits, R. G., Collins, W. J., Hand, M., Dutch, R., and Payne, J.: A Proterozoic Wilson cycle identified by Hf isotopes in central Australia: Implications for the assembly of Proterozoic Australia and Rodinia, *Geology*, 42, 231-234, [10.1130/g35112.1](https://doi.org/10.1130/g35112.1), 2014.
- Spaggiari, C. V., Bodorkos, S., Barquero-Molina, M., Tyler, I. M., and Wingate, M. T. D.: Interpreted bedrock geology of the south Yilgarn and central Albany-Fraser orogen, Western Australia, *Geological Survey of Western Australia, Record*, 10, 84, 2009.
- Spaggiari, C. V., Kirkland, C. L., Smithies, R. H., Wingate, M. T. D., and Belousova, E. A.: Transformation of an Archean craton margin during Proterozoic basin formation and magmatism: The Albany-Fraser Orogen, Western Australia, *Precambrian Research*, 266, 440-466, <https://doi.org/10.1016/j.precamres.2015.05.036>, 2015.
- Stark, J. C., Wang, X.-C., Li, Z.-X., Rasmussen, B., Sheppard, S., Zi, J.-W., Clark, C., Hand, M., and Li, W.-X.: In situ U-Pb geochronology and geochemistry of a 1.13 Ga mafic dyke suite at Bungar Hills, East Antarctica: The end of the Albany-Fraser Orogeny, *Precambrian Research*, 310, 76-92, <https://doi.org/10.1016/j.precamres.2018.02.023>, 2018.
- Tillberg, M., Drake, H., Zack, T., Högalm, J., and Åström, M.: In Situ Rb-Sr Dating of Fine-grained Vein Mineralizations Using LA-ICP-MS, *Procedia Earth and Planetary Science*, 17, 464-467, <https://doi.org/10.1016/j.proeps.2016.12.117>, 2017.
- Tillberg, M., Drake, H., Zack, T., Kooijman, E., Whitehouse, M. J., and Åström, M. E.: In situ Rb-Sr dating of slickenfibres in deep crystalline basement faults, *Scientific Reports*, 10, 562, [10.1038/s41598-019-57262-5](https://doi.org/10.1038/s41598-019-57262-5), 2020.
- Tyler, I. M., Spaggiari, C. V., Occhipinti, S. A., Kirkland, C. L., and Smithies, R. H.: Tropicana translated—late Archean to early Paleoproterozoic gold mineralization in the Albany-Fraser Orogen, GSWA 2015 extended abstracts: promoting the prospectivity of Western Australia. Geological Survey of Western Australia, 36-40, 2015.
- Vanhaecke, F., De Wannemacker, G., Balcaen, L., and Moens, L.: The use of dynamic reaction cell ICP mass spectrometry to facilitate Rb-Sr age determination, Geological Society, London, Special Publications, 220, 173-181, 2003.
- Villa, I. M., De Bièvre, P., Holden, N. E., and Renne, P. R.: IUPAC-IUGS recommendation on the half life of <sup>87</sup>Rb, *Geochimica et Cosmochimica Acta*, 164, 382-385, <https://doi.org/10.1016/j.gca.2015.05.025>, 2015.
- Wang, X.-C., Li, Z.-X., Li, J., Pisarevsky, S. A., and Wingate, M. T. D.: Genesis of the 1.21 Ga Marnda Moorn large igneous province by plume-lithosphere interaction, *Precambrian Research*, 241, 85-103, <https://doi.org/10.1016/j.precamres.2013.11.008>, 2014.
- The Marnda Moorn LIP, A Late Mesoproterozoic Large Igneous Province in the Yilgarn Craton, Western Australia July 2005 LIP of the Month (unpub), 2005.
- Woodhead, J. D., and Hergt, J. M.: Strontium, neodymium and lead isotope analyses of NIST glass certified reference materials: SRM 610, 612, 614, *Geostandards Newsletter*, 25, 261-266, 2001.



- 600 Zack, T., and Hogmalm, K. J.: Laser ablation Rb/Sr dating by online chemical separation of Rb and Sr in an oxygen-filled reaction cell, *Chemical Geology*, 437, 120-133, <https://doi.org/10.1016/j.chemgeo.2016.05.027>, 2016.
- Zack, T., and Kooijman, E.: Petrology and Geochronology of Rutile, *Reviews in Mineralogy and Geochemistry*, 83, 443-467, 10.2138/rmg.2017.83.14, 2017.
- Zussman, J.: The crystal chemistry of the micas, *Bulletin de Mineralogie*, 102, 5-13, 1979.

605

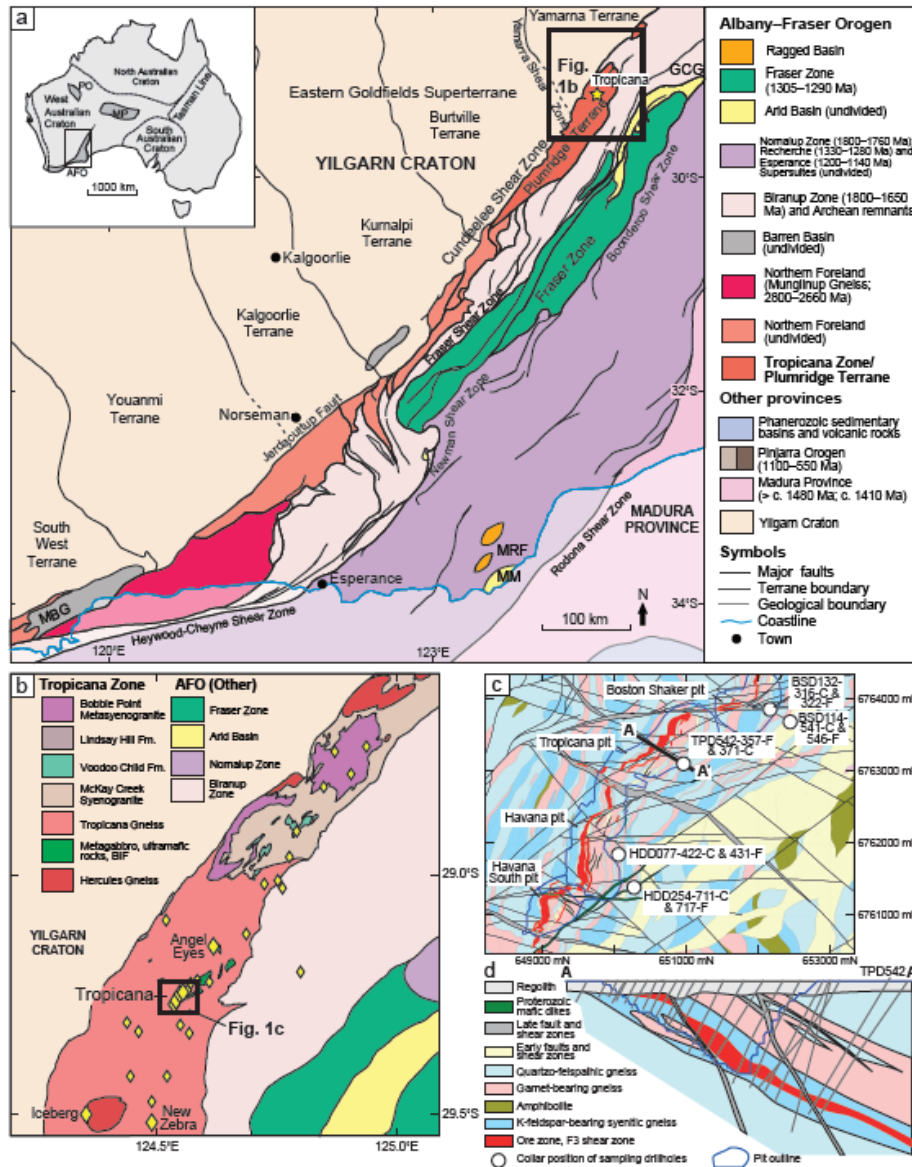
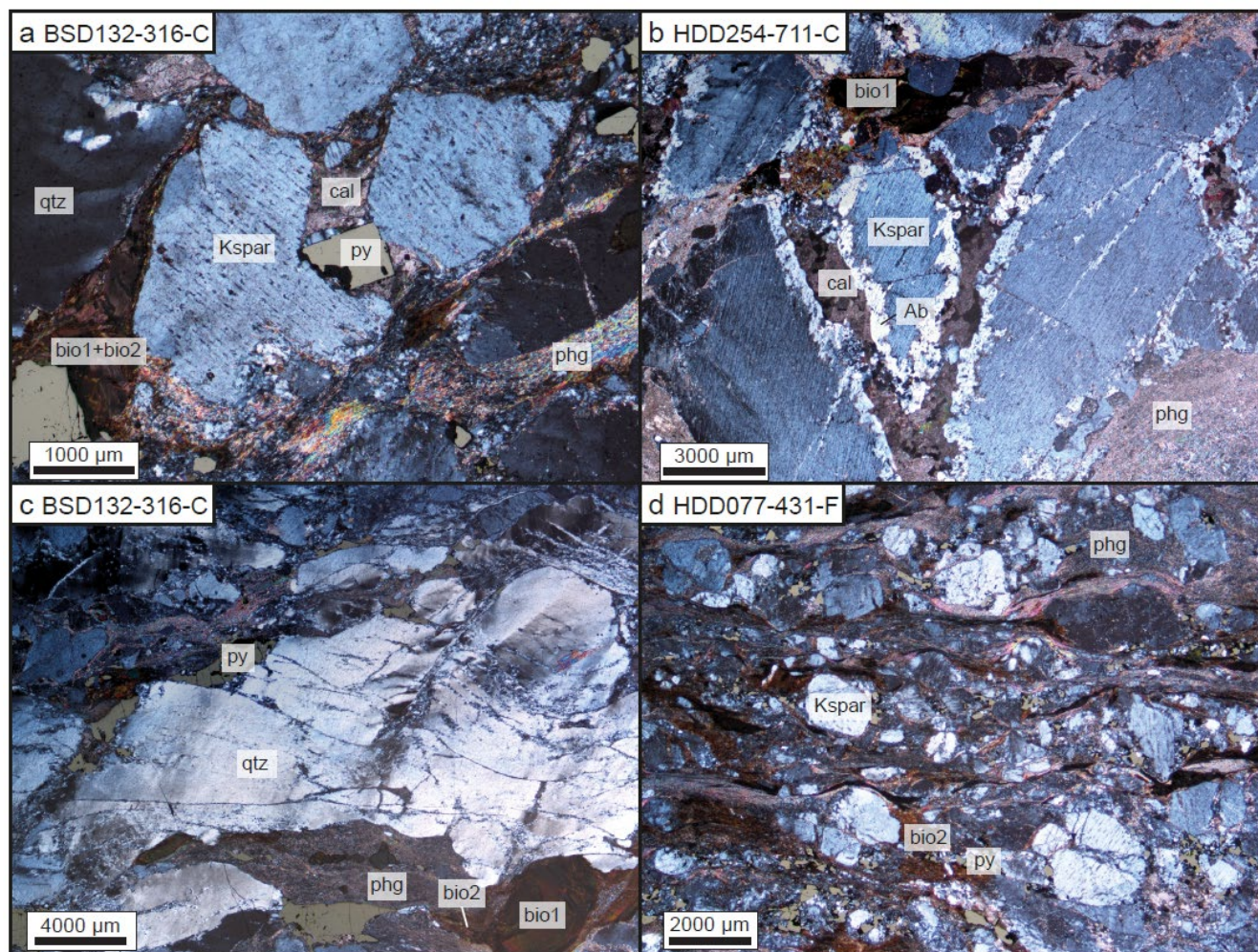
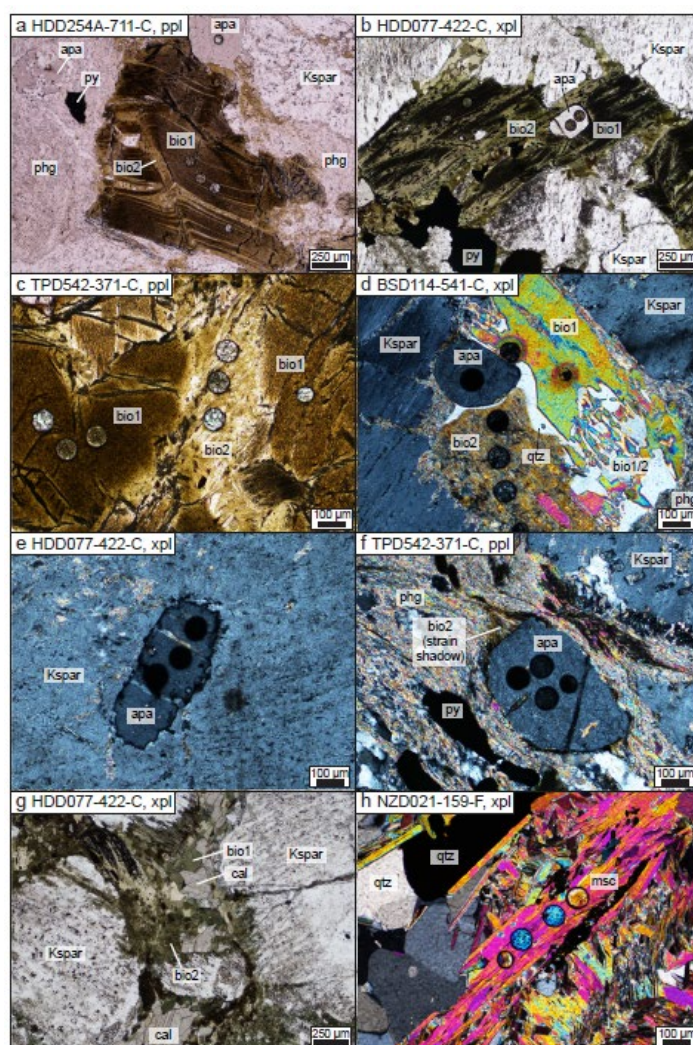


Fig. 1: (a) Simplified, pre-Mesozoic interpreted bedrock geology of the Albany–Fraser Orogen, modified from Spaggiari et al. (2015),  
 610 Doyle et al. (2015) and Scibiorski et al. (2016). Abbreviations: GCG—Gwynne Creek Gneiss; MBG—Mount Barren Group; MM—  
 Malcolm Metamorphics; MRF—Mount Ragged Formation; WF—Woodline Formation. (b) Interpreted basement map of the  
 Tropicana Zone/Plumridge Terrane, modified from Kirkland et al. (2015). Gold deposits and prospects are shown from the  
 Geological Survey of Western Australia MINEDEX database, with studied locations labelled. (c) Interpreted basement map of the  
 615 Tropicana gold mine from internal AngloGold Ashanti maps, showing locations of drill holes analyzed in this study. Note the  
 Tropicana and Havana pits have now joined. (d) Interpreted cross-section across the ore-bearing and F3 shear zone of the Tropicana  
 gold mine from AngloGold Ashanti, showing locations of drill holes (pale grey lines). All maps use GDA 1994 geodetic datum with  
 (c) using MGA zone 51 projection.



620 Fig. 2: Dual transmitted and reflected light, cross-polarized photomicrographs showing characteristic low-strain (a–c) and high-  
strain (d) microstructures and mineral relationships of studied samples. (a) Sample BSD132-316-C shows fractured perthitic  
feldspar from Assemblage 1 in the centre with carbonate, pyrite and quartz from Assemblage 2 filling the fracture. Quartz and  
biotite 1 show formation of sub-grains (Biotite 2). (b) Sample HDD254A-711-C, a carbonate from Assemblage 2 fills shear fractures  
that crosscut perthitic feldspar from Assemblage 1. Reaction rims along fractures show breakdown of perthite to albite. (c) Sample  
BSD132-316-C shows brittle–ductile deformation of large quartz and biotite 1 (bottom right) grains and precipitation of pyrite in  
625 strain shadows. (d) Sample HDD077-431-F shows porphyroclasts of perthitic feldspar within a mylonitic matrix consisting of biotite  
2, quartz, carbonate, pyrite and sericite.



630 Fig. 3: Thin section photomicrographs in transmitted light showing detailed mineral. (a) Biotite 2 recrystallized sub-parallel to axial  
plane of folded biotite 1, situated in association with phengite and interstitial to K-feldspar phenocrysts, from HDD254A-711-C. (b)  
Biotite 1 variably recrystallized to biotite 2, and associated with pyrite and apatite, all interstitial to K-feldspar phenocrysts from  
HDD077-422-C. (c) Recrystallized biotite 2 corridor between biotite 1 in TPD542-371-C. (d) Biotite in various stages of  
recrystallization, from euhedral biotite 1 to partly recrystallized biotite 1/2 to fully recrystallized biotite 2, from BSD114-541-C. Note  
association of unstrained quartz with recrystallization. (e) Apatite (magmatic?; ?) fully enclosed in K-feldspar phenocryst from  
HDD077-422-C. (f) Apatite (2) porphyroblast with rare strain shadow of biotite 2 and phengite, implying locally biotite 2 > apatite  
> phengite, from TPD542-371-C. Also note close association of pyrite. (g) Carbonate ingress with recrystallization of biotite 1  
to biotite, interstitial to K-feldspar from HDD077-422-C. (h) euhedral muscovite in association with quartz, from NZD021-159-F. apa  
= apatite, bio1 = euhedral, first generation biotite, bio1/2 = partly recrystallized biotite 1, bio2 = recrystallized biotite 1, cal = calcite,  
Kspar = K-feldspar, msc = muscovite, phg = phengite, py = pyrite, qtz = quartz, ppl = plane-polarized, xpl = cross-polarized. Circular  
640 holes are laser ablation pits of 87 or 60 μm diameters.

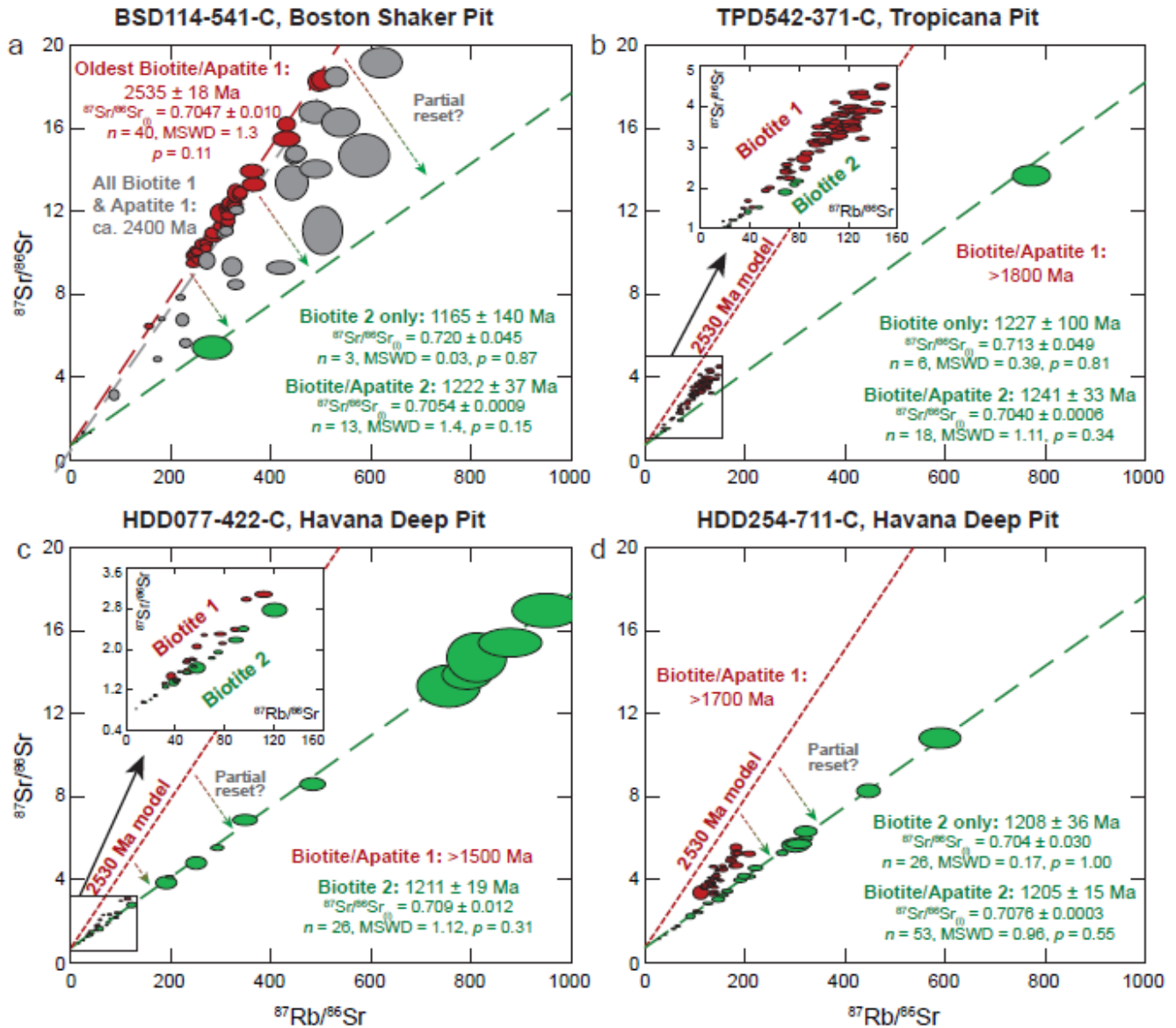
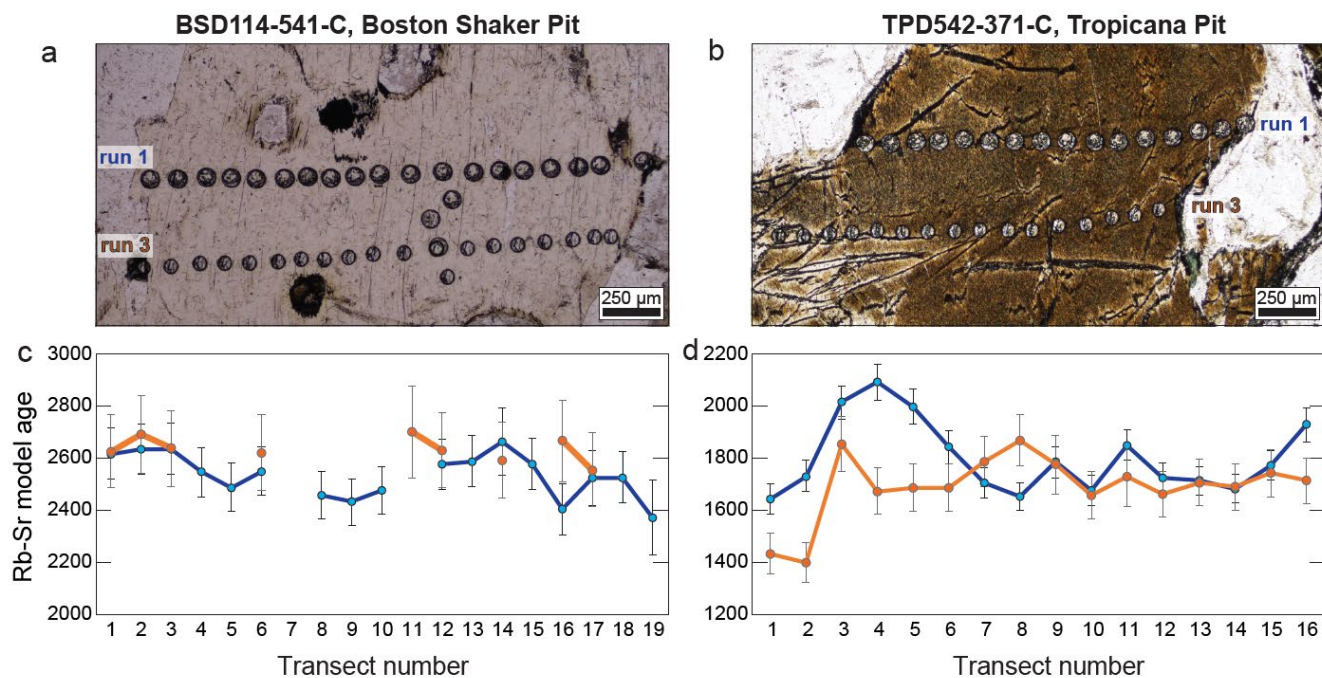


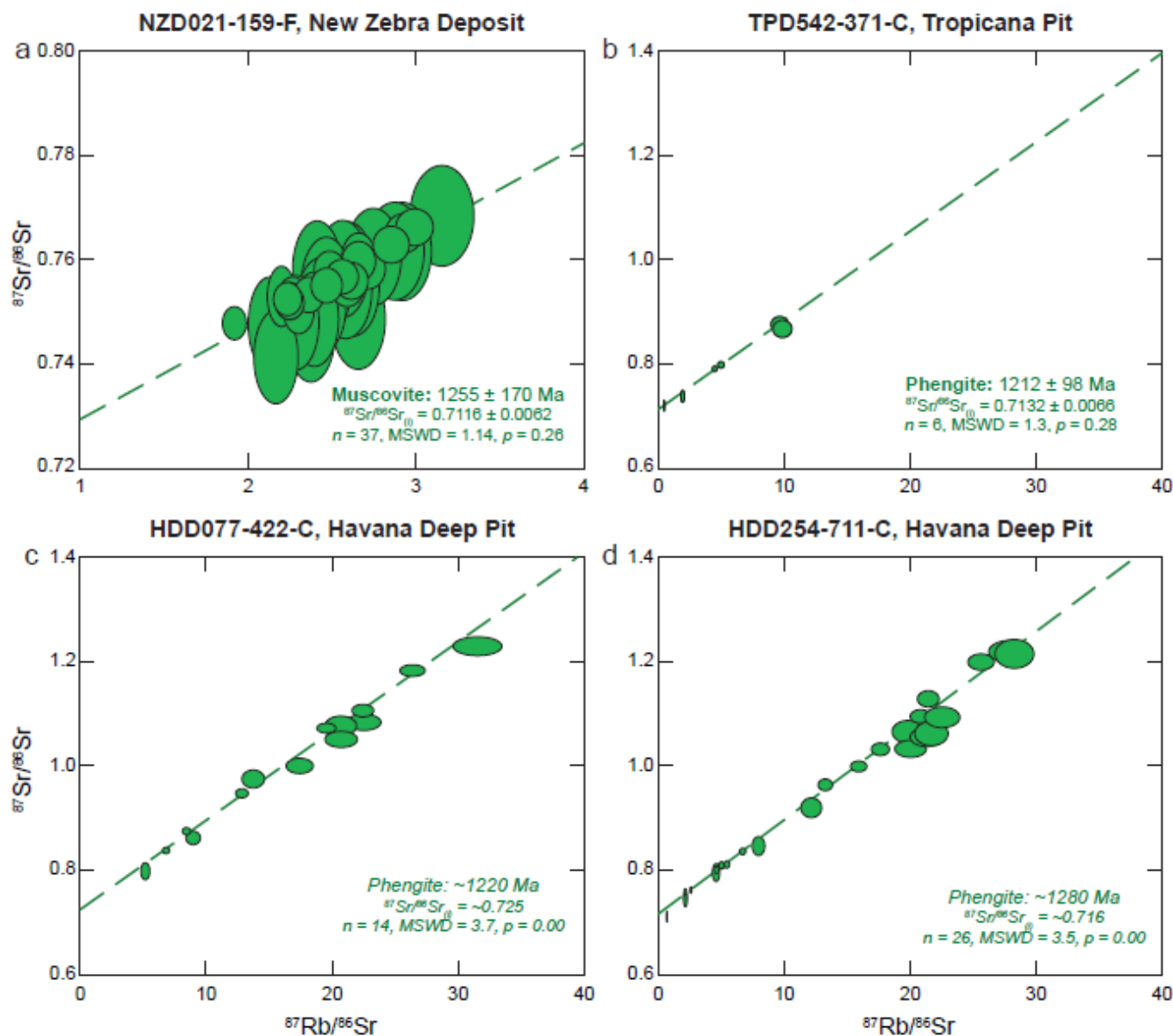
Fig. 4: Biotite Rb–Sr isochrons for individual samples, with red data corresponding to assemblage 1 and green data corresponding to assemblage 2 biotite. Grey data is considered to be part of assemblage 1 but with loss of radiogenic Sr. All error ellipses are plotted at  $2\sigma$ . The 2530 Ma model age is based off Fig. 4a, assuming an initial  $^{87}\text{Sr}/^{86}\text{Sr}$  of 0.7045. Note that for assemblage 2, ages are calculated both solely with biotite 2 and with biotite 2 and apatite combined (see section 3 and discussion).

645





**Fig. 5: Transects across two large, euhedral biotite grains. (a, b) Transmitted, plane-polarized photomicrographs of part of the euhedral grains, showing 87 µm (run 1) and 64 µm (run 3) laser ablation pits along the grains. (c, d) Rb-Sr model ages for each spot in the transect across two runs. Model ages were computed using  $^{87}\text{Sr}/^{86}\text{Sr}$  of apatite 1 in corresponding sample (see Fig. 7).**



650

Fig. 6: Phengite and muscovite Rb-Sr isochrons for individual samples, with green data corresponding to assemblage 2 phengite or muscovite. All error ellipses are plotted at  $2\sigma$ . Ages in italics are estimates only due to overdispersion for a single population.

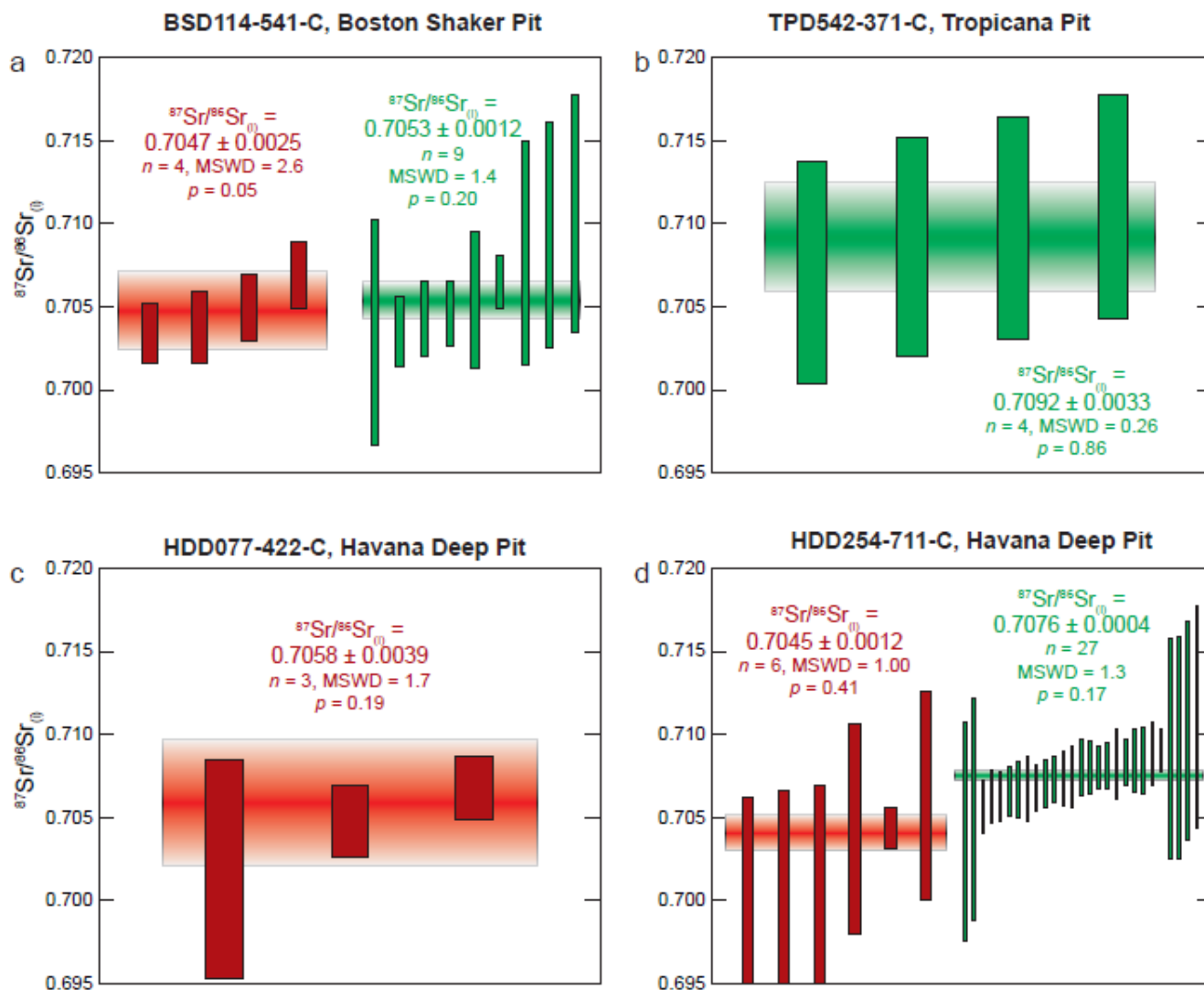
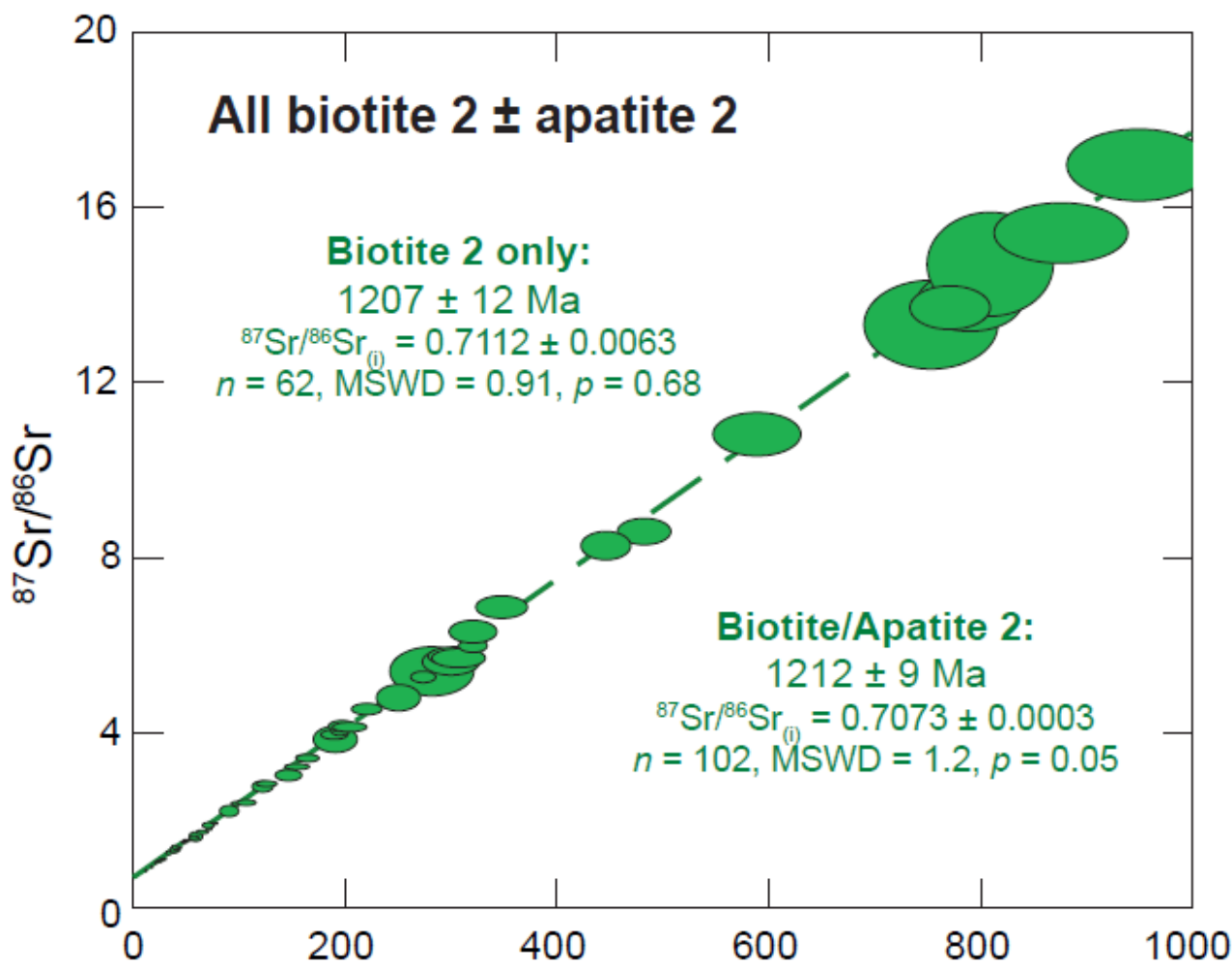
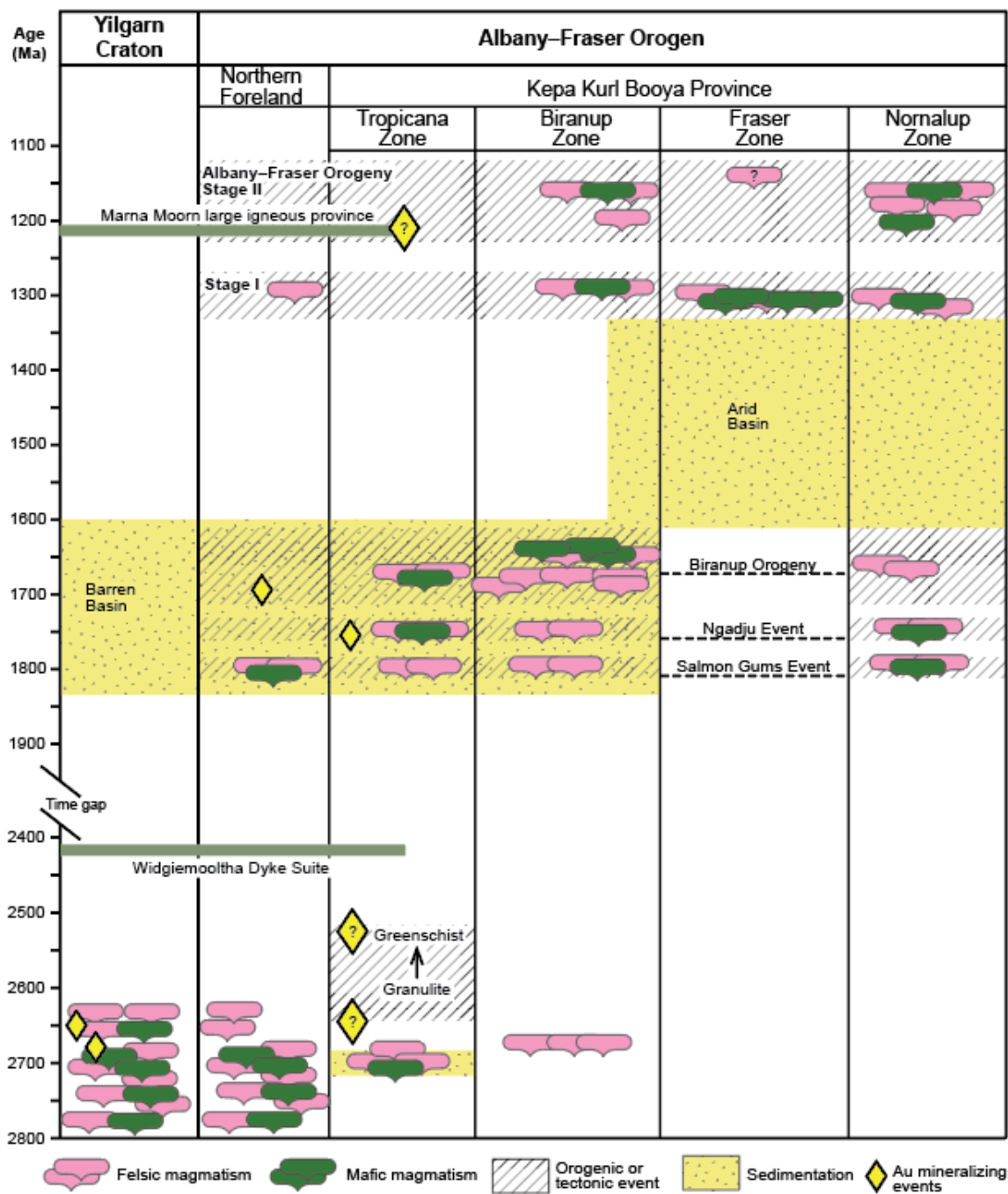


Fig. 7: Apatite weighted mean  $^{87}\text{Sr}/^{86}\text{Sr}$ . Due to the lack of Rb in apatite, measured  $^{87}\text{Sr}/^{86}\text{Sr}$  values can be considered as initial ratios.



655

Fig. 8: Combined isochron of biotite 2 analyses from all four samples in the Tropicana gold mine, computed with and without apatite 2.



660 Fig. 9: Synthetic time–space plot showing geological history of the Tropicana Zone, modified from Spaggiari et al. (2015) and Kirkland et al. (2015). The timing of mineralization in the Tropicana Zone is uncertain (see discussion).



Deposit/pit	Easting (m)	Northing (m)	RL (m)	Sample ID	Assemblage	Main minerals	Rb-Sr phases	Dated sessions
Boston Shaker	6763834	652321	354	BSD 132-316-C	1	Coarse-grained quartz, K-feldspar; medium-grained pyrite; fine-grained apatite, monazite; interstitial biotite, (Fe-rich) calcite, phengite	Biotite 1/2, Phengite	-
Boston Shaker	6763834	652321	354	BSD 132-322-F	2	Medium-grained perthitic K-feldspar, albite, pyrite, quartz; quartz veining; interstitial (Fe-rich) calcite, phengite and biotite	Biotite 1/2, Phengite	-
Boston Shaker	6763644	652657	348	BSD 114-541-C	1	Coarse-grained K-feldspar; medium-grained plagioclase; apatite; interstitial biotite, quartz, actinolite; fine-grained pyrite	Biotite 1/2, Phengite, Apatite 1/2	1,3
Boston Shaker	6763644	652657	348	BSD 114-546-F	2	Medium-grained plagioclase, quartz; fine-grained pyrite, ankerite, foliation-parallel phengite	Biotite 1/2, Phengite	-
Tropicana	6763087	651144	344	TPD 542-357-F	2	Strongly foliated, defined by fine-grained plagioclase, pyrite, biotite and phengite; rare quartz, calcite and apatite	Biotite 1/2, Phengite	-
Tropicana	6763087	651144	344	TPD 542-371-C	1	Coarse-grained K-feldspar, medium-grained biotite, apatite, plagioclase, quartz; fine-grained pyrite; interstitial biotite, phengite	Biotite 1/2, Phengite, Apatite 2	1,3
Havana	6761694	650183	362	HDD 077-422-C	1	Coarse-grained (perthitic) K-feldspar; medium-grained plagioclase; fine-grained apatite, pyrite, zircon; interstitial biotite, phengite, quartz	Biotite 1/2, Phengite, Apatite 1	1,3
Havana	6761127	650536	362	HDD 254-711-C	1	Coarse-grained (perthitic) K-feldspar; medium-grained plagioclase, apatite, quartz, pyrite; interstitial biotite, phengite, dolomite	Biotite 2, Apatite 1/2	1,2,3
Havana	6761127	650536	362	HDD 254-717-F	2	Medium-grained K-feldspar, quartz; fine-grained plagioclase, pyrite, apatite, dolomite; interstitial biotite, phengite	Biotite 1/2, Phengite, Apatite 2	-
New Zebra	6730709	642098	382	NZD 021-159-F	2	Parasitically folded defined by quartz and muscovite; ankerite and calcite abundant; minor fine-grained rutile, pyrite, albite, apatite	Muscovite	1,3
Iceberg	6733203	634266	385	IBD 004-76-F	2	Strongly foliated, foliation defined by quartz, altered plagioclase, phengite, fine-grained pyrite	Phengite	-
Angel Eyes	6772309	657438	316	AERC 012D-156-F	2	Strongly foliated, two zones. Upper zone: medium-grained quartz; interstitial phengite, ankerite, pyrite. Lower zone: very fine-grained quartz, phengite, pyrite and ankerite, apatite	Phengite, Apatite 2	-

**Table 1:** List of samples dated in this study. TGM = Tropicana gold mine. C = Coarse-grained. F = Fine-grained. Rb/Sr phases indicates the minerals that were dated in each sample, with 1 and 2 corresponding to assemblage 1 and 2, respectively. Eastings, Northings and Reduced Level (RL = Z) are in GDA 1994, MGA zone 51 projection for the drill hole collar.



665 **Supplementary Table A: Rb-Sr geochronology parameters during the three analytical sessions.**

**Supplementary Table B: Compendium of Rb-Sr data, including unknowns and reference materials.**

670 **Supplementary Fig. A: Graphic illustration of how a reaction cell sandwiched between two quadrupoles separates Rb from Sr isotopes, as well as deals with interfering ions.**

675 **Supplementary Fig. B: Compilation of (i) core photos, (ii) transmitted, plane-polarized light image of full thin section, (iii) transmitted, cross-polarized light image of full thin section, and (iv) automated mineral analysis image of full thin sections, accompanied by legend. Yellow line in core photos indicates approximate position of thin section billet. All thin sections are  $46 \times 27$  mm.**

680 **Supplementary Fig. C: Rb-Sr isochron showing identical ages within uncertainty between sessions 1, 2 and 3 for biotite 2 from HDD254-711-C (Tropicana, WA) and biotite from CK001B (Finnmark, Norway). Spots for these analyses were collected adjacent to each other (see Fig. 2 for examples). Ages for CK001B overlap with ages obtained by Rb-Sr solution ages ([Kirkland et al., 2007](#)).**